Iowa Research Online
The University of Iowa's Institutional Repository

University of Iowa
Iowa Research Online

Theses and Dissertations

Summer 2017

MRI fat-water separation using graph search based methods

Chen Cui
University of Iowa

Follow this and additional works at: https://ir.uiowa.edu/etd

 Part of the Electrical and Computer Engineering Commons

Copyright © 2017 Chen Cui

This dissertation is available at Iowa Research Online: https://ir.uiowa.edu/etd/5740

Recommended Citation
Cui, Chen. "MRI fat-water separation using graph search based methods." PhD (Doctor of Philosophy) thesis, University of Iowa, 2017.
https://doi.org/10.17077/etd.as18ob1b

Follow this and additional works at: https://ir.uiowa.edu/etd

 Part of the Electrical and Computer Engineering Commons

www.manaraa.com

MRI FAT-WATER SEPARATION USING GRAPH SEARCH BASED METHODS

by

Chen Cui

A thesis submitted in partial fulfillment of the
requirements for the Doctor of Philosophy
degree in Electrical and Computer Engineering
in the Graduate College of
The University of Iowa

August 2017

Thesis Supervisor: Associate Professor Mathews Jacob

www.manaraa.com

Graduate College
The University of Iowa
Iowa City, Iowa

CERTIFICATE OF APPROVAL

PH.D. THESIS

This is to certify that the Ph.D. thesis of

Chen Cui

has been approved by the Examining Committee for the thesis requirement for the Doctor of Philosophy degree in Electrical and Computer Engineering at the August 2017 graduation.

Thesis Committee: _____
Mathews Jacob, Thesis Supervisor

_____
Vincent A Magnotta

_____
Daniel Thedens

_____
Mona Garvin

_____
Xiaodong Wu

www.manaraa.com

ACKNOWLEDGEMENTS

Five years of research, six exciting seasons of playing soccer in the Kicker's League in Iowa City, seven years of persistence, consistent support and supervision from my advisor and personal growth are the key words of the 'life thesis' I have been writing over the past seven years . This has been nothing less than a journey of self discovery and adventure. Now, finally I am writing my PhD thesis to touch the finish line and sincerely acknowledge the support, encouragement and guidance I have received, without which completing my PhD would never have been a reality.

First and foremost, I would like to thank Dr. Mathews Jacob for being my research advisor since 2012. It has been my great honor and fortune to work with you from day to day. Your clarity, calibration and passion in research have been the best learning resources for me. I will always remember you took the extra time and patience to explain different research topics in great details to me, quite often repeatedly. I will also remember your encouragement to take more ownership of my own work and activley look for collaboration with colleagues both in and out of our group. My sincere gratitude to you for being my doctoral research thesis supervisor.

Next, I would like to thank Dr. Xiaodong Wu, Dr. Vincent Magnotta, Dr. Mona Garvin and Dr. Daniel Thedens for serving on my dissertation committee. It has been my honor and pleasure to have you all in my dissertation committee and I sincerely thank you for your invaluable guidance throughout this process, your ideas, and feedback. I would also like to thank Dr. John Newell for his contribution to this thesis work and for his encouragement during our meetings. Same gratitude to

www.manaraa.com

Abhay Shah for the research collaboration. The joint effort is what I have enjoyed the most.

I would like to thank my present and past labmates in Computational Biomedical Imaging Group - Sajan Goud Lingala, Yue Hu, Xuan Zhou, Ipshita Bhattacharya, Sunrita Poddar, Sampada Bhave, Arvind Balachandrasekaran, Sampurna Biswas, Greg Ongie, Yasir Mohsin, Merry Mani, Hemant Aggarwal, Ankit Parekh for a very friendly and collaborative environment in the lab.

I am also thankful to the ECE department. It is the department who gave me the opportunity to come to study at the University of Iowa and it has been changing my life on both professional and personal levels. I have had the great opportunity to take courses from professors in the department and learn about their research work through various talks and personal conversations. I would also like to thank Cathy and Dina for their support throughout these years. Their rich experiences in working with graduate students in the department have been of great help in my completion of degree. I also made many great friends in the department. Many thanks to Ray, Hu Qiao, Jin Dakai, Zhang Li, Li Cheng, Chen Cheng, Chen Zhi, and Wang Yichao for supporting me in both study and life.

I would also like to give special thanks to Ms. Emily Roberts and the John Pappajohn Entrepreneurial Center. I had the opportunity to get to know the entreprenuerial world outside my research work. It has been a fulfilling, fun and precious journey to work on Western Wise. I will never forget our pitch to Mr. John Pappajohn, the trip to Utah and the days and nights we worked hard on the venture.

www.manaraa.com

I would like to thank all my friends here in Iowa City for all the favors, support, encouragement, discussions and good times throughout these years. Your kindness and tolerance have strengthened me every single day.

I would like to express my gratitude to my girlfriend Jennifer Dibbern for the constant openness, presence and love in my life for the past two years. Thanks for being there whether I was having joy or challenges in life. I also learned a lot by obsering your dedication to work, initiative in life and the genuineness to people.

Finally, I would like to dedicate this dissertation to my parents. Thank you, mom and dad for believing in me and always encouraging me to find my own path in life. I can never express in enough words how thankful I am for all your support, sacrifices and love. I would never have been able to do this without you. I love you both and hope this precious milestone in my life, brings you pride.

www.manaraa.com

ABSTRACT

The separation of water and fat from multiecho images is a classic problem in magnetic resonance imaging (MRI) with a wide range of important clinical applications. For example, removal of fat signal can provide better visualization of other signals of interest in MRI scans. In other cases, the fat distribution map can be of great importance in diagnosis.

Although many methods have been proposed over the past three decades, robust fat water separation remains a challenge as radiological technology and clinical expectation continue to grow. The problem presents three key difficulties: a) the presence of B0 field inhomogeneities, often large in the state-of-the-art research and clinical settings, which makes the problem non-linear and ill-posed; b) the ambiguity of signal modeling in locations with only one metabolite (either fat or water), which can manifest as spurious fat water swaps in the separation; c) the computational expenditure of fat water separation methods as the size of data is increasing along with the evolving MRI hardware, which hampers the clinical applicability of fat water separation.

The main focus of this thesis is to develop novel graph search based algorithms to estimate the B0 field inhomogeneity maps and separate fat water signals with global accuracy and computational efficiency. We propose a new smoothness constrained framework termed as the GlObally Optimal Surface Estimation (GOOSE), in which the spatial smoothness of the B0 field is modeled as a finite constraint between adjacent voxels in a uniformly discretized graph. We further develop a new

www.manaraa.com

non-equidistant graph model that enables a Rapid GlObally Optimal Surface Estimation (R-GOOSE) in a subset of the fully discretized graph in GOOSE. Extensions of the above frameworks are also developed to achieve high computational efficiency for processing large 3D datasets. Global convergence of the optimization formulation is proven in all frameworks. The developed methods have also been compared to the existing state-of-the-art fat water separation methods on a variety of datasets with consistent performance of high accuracy and efficiency.

www.manaraa.com

PUBLIC ABSTRACT

In vivo magnetic resonance imaging (MRI) has been widely used in the clinical setting and radiological research. Since it is radiation free and can provide images of high quality, it has played a promising and increasingly active role in medicine overall. Most clinical MRI applications collect signal from protons, either as part of water or fat. By applying different imaging schemes and acquisition times, MRI can provide excellent contrast between soft tissues based on whether the signal is from water protons or fat ones.

Due to the difference between biochemical structures of fat and water, fat signal can appear bright in many important imaging scenarios and therefore obscure underlying pathology such as inflammation, edema or progression of certain tumor. Meanwhile, direct visualization of fat distribution is also desirable in various pathologies such as fatty tumors, including adrenal adenomas, angiomyolipomas and other fat-related mesenchymal tumors. Quantification of visceral adipose tissue is also enjoying a great interest in recent studies. In these cases, separation of water and fat signals can be highly useful by providing water-only and/or fat-only images.

However, the separation of fat and water signals in MRI remains difficult due to multiple hurdles. The mathematical model for the fat water signal is flawed by nature in the presence of fat- or water-only locations. On the other hand, while technology advancement in the MRI scanner is bringing more promising diagnosis and treatment plans for patients, it also poses challenges in redesigning current fat water separation methods for the advancement. Large B0 magnetic field variations

www.manaraa.com

can make the separation problem more ill-conditioned. The increasing data size and resolution demand faster, simpler and more accurate approaches to solve the fat water separation problem.

The goal of this thesis is to develop new fat water separation methods by employing graph search based models. The developed methods achieve global optimality of the newly designed problem formulations for fat water separation. New frameworks are also proposed in this work to reduce the computational time by an order of magnitude compared to state-of-the-art methods. With experiments on a variety of datasets, particularly with challenging anatomical regions and of large size, the proposed methods have demonstrated their great potential to improve the state-of-the-art methods in more applications of MRI fat water separation.

www.manaraa.com

TABLE OF CONTENTS

www.manaraa.com

www.manaraa.com

LIST OF TABLES

www.manaraa.com

www.manaraa.com

LIST OF FIGURES

Figure

www.manaraa.com

www.manaraa.com

www.manaraa.com

www.manaraa.com

www.manaraa.com

www.manaraa.com

www.manaraa.com

CHAPTER 1
INTRODUCTION

1.1 Fat Water Separation in MRI: Development and Motivation

Magnetic Resonance Imaging (MRI) is a non-invasive imaging modality based on the principles of nuclear magnetic resonance (NMR). Since the early development in the 1970s, MRI has demonstrated to be a highly versatile and multi-functional imaging technique. It is estimated that there are more than 36,000 MRI scanners in use worldwide for diagnostic medicine and biomedical research [1]. Unlike other imaging modalities like positron emission tomography (PET) and computed tomography (CT) which involve radiation, MRI applies strong magnetic fields, radio waves and field gradients to generate images of the organs in the body and hence does not require body exposure to ionizing radiation. While X-rays provide detailed information about high density structures like bones, MRI provides images with high resolution of soft tissues and anatomical structures with high contrast.

Most clinical MRI images are signals collected from water and/or fat protons. The separation of water and fat signals in MRI is an important problem with many clinical applications [2–6]. For example, fat removal is the objective of many cases. It is very typical in pulse sequences such as steady-state free precision (SSFP) [6–9], spoiled gradient echo (SPGR) [10–14], or fast spin echo(FSE) [15–18], where fat can appear lunimous and therefore may disguise the underlying pathologies. On the other hand, fat can also be the target signal of interest for different study purposes

www.manaraa.com

such as fatty infiltrative diseases [19, 20], adenoma [21] or renal angiomyolipomas [22]. The quantification of fat signal is also drawing great interest in many studies visceral adipose tissue [23,24], brain [25], breast [26], liver [5,27–30], cardio-ventricular diseases [31–33]. In these cases, the fat-only images can bring desirable insights to the diagnosis.

Researchers have proposed a variety of methods to address the fat water separation problem. Overall, there are two major types of the various methods. The first type, also a straightforward approach, is fat suppression during excitation. A common practice is to employ frequency selective excitation/saturation schemes such as CHESS [34], simultaneous spatial and spectral excitation [35,36] or short T1 inversion recovery sequences [37], since protons from water and fat are excited at different resonance frequencies. The advantages of this type methods are fat are removed during the data collection stage without requiring any post processing steps during image reconstruction or analysis. However, the main downside is many of them are innately sensitive to B0 inhomogeneities. Due to the magnet imperfections and susceptibility of the imaging object, B0 inhomogeneities are often unavoidable in the imaging process. This often gives rise to frequency shifts in spatial dimensions which eventually represent as geometry distortion or intensity change in MRI images. In the case of frequency selective excitation scheme, B0 inhomogeneities can lead to the failure of fat signal suppression or even the suppression of water signal in certain conditions.

The other type of methods is so called chemical shift encoded fat water imaging. In this type, a series of images are collected in a sequential order at multiple time

www.manaraa.com

echo (TE) (also called multiecho methods). Each pixel in the images is considered as a combination of fat and water signals, both of which contain the complex valued magnitude and phase components. This is the basic signal model used in the famous Dixon method [38] and its many variations. The separate fat and water signals, often as well as an estimation of the B0 inhomogeneity map are obtained by fitting the model to the collected measurements often with different post processing strategies such as analytical models, morphological methods, energy minimization formulations or hyrid schemes. The main benefit of these methods are their capability of generating fat- and water-only images, whic can be of great value in clincal settings as mentioned above [10,23,24]. Another advantage is the insensitivity to B0 inhomogeneity. In fact, most of these methods can provide an estimate of the B0 inhomogeneity map in addition to the separate fat and water images. The estimated B0 inhomogeneity map (also called 'field map') are also seen to gain more attention in recent studies such as quantitative susceptibility mapping (QSM) [39].

Because of the advantages of the Dixon based methods and their clinical and research applications, a plethora of methods for field map estimation and fat water separation have been proposed over the last three decades. In the next chapter, the Dixon model and different methods with their merits and drawbacks will be further elaborated before introducing the main methods proposed in this thesis.

www.manaraa.com

1.2 Overview of Contributions

The main goal of this thesis is to develop novel frameworks for field map estimation and fat water separation with high accuracy and efficiency. In particular, the main contributions of the thesis are the following:

1. A smoothness constrained problem formulation to estimate field inhomogeneity: Field map estimation is reformulated as a constrained surface estimation problem to exploit the spatial smoothness of the field, thus minimizing the ambiguities in the recovery. Specifically, the differences in the field map-induced frequency shift between adjacent voxels are constrained to be in a finite range. The discretization of the above problem yields a graph optimization scheme, where each node of the graph is only connected with few other nodes in a fully discretized graph.

2. A non-iterative graph search solution with global optimality: We introduced a non-iterative graph search algorithm for solving the above smoothness constrained formulation. The global minimum of the constrained optimization problem is guaranteed with theoretical proof. This non-iterative graph search model greatly reduces the dependency on parameter initialization and tuning in many state-of-the-art iterative methods. The global optimality and freedom from iterative restrictions lead a significant improvement in performance accuracy and stablity.

3. A non-equidistant graph model with high computational efficiency: As a gener-

www.manaraa.com

alization of the fully discretized non-iterative graph scheme, a new non-equidistant graph model is futher proposed to solve a smoothness penelized likelihood cost function. The optimal surface search for field map at each voxel is conducted in a subset of the uniformly discretized field values, which are the local minimizers of the voxel independent maximum likelihood cost function. The accommodation of only local minima set significantly reduces the graph connectivity, which further decreases the computational time by an order of magnitude.

4. A multi-resolutional framework for the non-equidistant graph search algorithm: A new multi-resolution framework to employ the non-equidistant graph search algorithm was developed in this work to further achieve computational gains. Global convergence of the predesigned cost function is consistently upheld in the framework. The new framework successfully achieved 50% time reduction in computational time compared to the initial non-equidistant graph model proposed above.

1.3 Thesis Organization

The structure of the thesis is as follows:

- **Chaper 2: Background:** The chapter provides an overview of the multi-echo fat water separation methods in MRI including the Dixon model and most relevant previously proposed methods for estimating B0 inhomogeneity map. In addition, basic concepts regarding the popular graph search framework will also be discussed in this chapter. Both these respective aspects form the build-

www.manaraa.com

ing blocks of the developed novel methods for graph based fat water imaging methods.

- **Chaper 3: Fat water separation using GlObally Optimal Surface Estimation (GOOSE):** This method models the field map estimation as a smoothness constrained optimization problem. The graph search is conducted in a fully discretized graph model with global optimality. A 3D extension of the proposed GOOSE is also introduced in this chapter. The proposed method and its extension are tested on various datasets for validation.

- **Chaper 4: Fat water separation using Rapid GlObally Optimal Surface Estimation (R-GOOSE):** The chapter describes the novel non-equidistant graph based method developed for fat water separation termed as Rapid GOOSE (R-GOOSE). In particular, we formulate the field map estimation as a 3D optimization problem, where the proposed global criterion is the sum of the voxel independent maximum likelihood measurement and a smoothness regularization penalty term.

- **Chaper 5: Fat water separation using multi-resolutional Rapid GlObally Optimal Surface Estimation (mR-GOOSE):** The chapter focuses on developing a new framework based on R-GOOSE that can further reduce the computational complexity, while still preserving the global convergence of the problem formulation. The smoothness regularized formulation in R-GOOSE was adopted but we further exploited the field map smoothness and the vicin-

www.manaraa.com

ity of the local minima in spatial neigborhood by creating a multi-resolutional pipeline in data flow.

- **Chaper 6: Conslusions:** This chapter provides summary of the thesis and discusses the possible directions of future work.

Each chapter in this thesis consists of various notations and formulations. In order to maintain consistency and ease of understanding for the reader, each chapter related to a specific aim of this thesis shall reformulate the problem mathematically. Certain terminologies are used interchangeably such as graph seach and optimal surface estimation, chemical shift encoded fat water imaging and multiecho fat water separation, fat water separation and fat water decomposition, as well as B0 inhomogeneity map and field map.

www.manaraa.com

CHAPTER 2
BACKGROUND

2.1 Introduction

In this chapter, we will first describe the Dixon model widely used for the multiecho fat water separation. Then we will introduce different methods previously proposed to solve for the Dixon model. We will mainly look at the most relavant approaches including the classic voxel independent methods, morphological strategies and the graph cut formulations. The last section describes the basic concepts of graph search as a preparation for next chapters.

2.2 Dixon-based Model

We now review the mathematical expression of the Dixon signal model that is essential for the discussion in later sections. In multiecho water and fat decomposition, a sequence of images are collected with different echo time (TE) shifts, $t_1, t_2, \ldots, t_N$. The signal at each individual voxel is described by the model in [40]:

$$s(\mathbf{r}, t_n) = \left(\rho_{\text{water}}(\mathbf{r}) + \rho_{\text{fat}}(\mathbf{r}) \left[\sum_{i=1}^{M} \beta_i \, e^{j2\pi\delta_i \, t_n} \right] \right) e^{-\gamma(\mathbf{r})t_n}, \quad n = 1, \ldots, N \tag{2.1}$$

Here, $\rho_{\text{water}}(\mathbf{r})$ and $\rho_{\text{fat}}(\mathbf{r})$ are complex-valued concentrations of water and fat, respectively. The fat signal is modelled using an M peak model, where δ_i is the chemical shift between the i^{th} fat peak and water, measured in Hz, and $\beta_i > 0$ is the relative weight of each peak. The relative weights add up to unity ($\sum \beta_i = 1$). The

www.manaraa.com

parameters β_i and δ_i are assumed to be known; the decomposition process involves the estimation of the unknown concentrations $\rho_{\text{fat}}, \rho_{\text{water}}$, as well as $f(\mathbf{r})$ and $T_2^*(\mathbf{r})$ from the measured data. The field inhomogeneity induced frequency shift and T_2^* decay terms are consolidated in the parameter $\gamma(\mathbf{r}) = [1/T_2^*(\mathbf{r}) - j2\pi f(\mathbf{r})]$. Here, $f(\mathbf{r})$ is the local frequency shift due to magnetic field inhomogeneity at the spatial location $\mathbf{r} = (x, y)$, while $T_2^*(\mathbf{r})$ models the decay due to intra-voxel dephasing. The consolidation of the T_2^* decays of fat and water into a single term is shown to reduce bias and improved noise stability [40, 41]. This model can be expressed in the matrix form as:

$$\underbrace{\begin{bmatrix} e^{-\gamma t_1} & e^{-\gamma t_1}\left(\sum_{i=1}^{M} \beta_i e^{j2\pi\delta_i t_1}\right) \\ .. & \\ e^{-\gamma t_n} & e^{-\gamma t_n}\left(\sum_{i=1}^{M} \beta_i e^{j2\pi\delta_i t_n}\right) \end{bmatrix}}_{\mathbf{A}_\gamma} \underbrace{\begin{bmatrix} \rho_{\text{water}} \\ \rho_{\text{fat}} \end{bmatrix}}_{\mathbf{g}} = \underbrace{\begin{bmatrix} s[1] \\ .. \\ s[N] \end{bmatrix}}_{\mathbf{s}}. \tag{2.2}$$

In the above equation, if the field inhomogeneity ($f(\mathbf{r})$) is known, or zero at all locations in an ideal scenario, the problem is linear and it is trivial to recover fat water concentrations ρ_{fat} and ρ_{water}. However, as mentioned in Chapter 1, B0 inhomogeneity is unavoidable due to the magnet imperfections and susceptibility artifacts. Therefore, the estimation of field map becomes the crux of solving for fat water separation. Specifically, it poses four challenges:

1. Non-linearity of the signal model: The field inhomogeneity appears in the exponential phase term $e^{-\gamma(\mathbf{r})t_n}$, making the problem ill-posed and the signal recovery

www.manaraa.com

non-trivial.

2. Ambiguity of the signal model: The signal model assumes both fat and water signals at each location. However, there are pixles in multiecho images with only fat or water component. In this case, only one of the two mathematical solutions is correct when the model is fitted to measurements. See an example in Figure 2.1.

3. Phase wrapping: The exponential phase term is periodic. Hence, there are more than one correct solution in the signal model for field map estimation. Then it requires additional constraints such as global smoothness of field map to determine the corrent solution.

4. Large range of B0 field inhomogeneity: The B0 field variations increase as the magnetic field strength continues to grow such as in 3T or above scanners. At the same time, in objects with internal cavities such as lung images, abrupt changes might appear in regions of transition between tissues and air. These strong variations in B0 field present additional challenges for the fat water separation problem.

2.3 Previously Proposed Methods

This section will review some of the most relevant methods for multiecho fat and water separation. A key factor that differentiates these methods is how the field smoothness assumption is formulated in the post processing steps.

www.manaraa.com

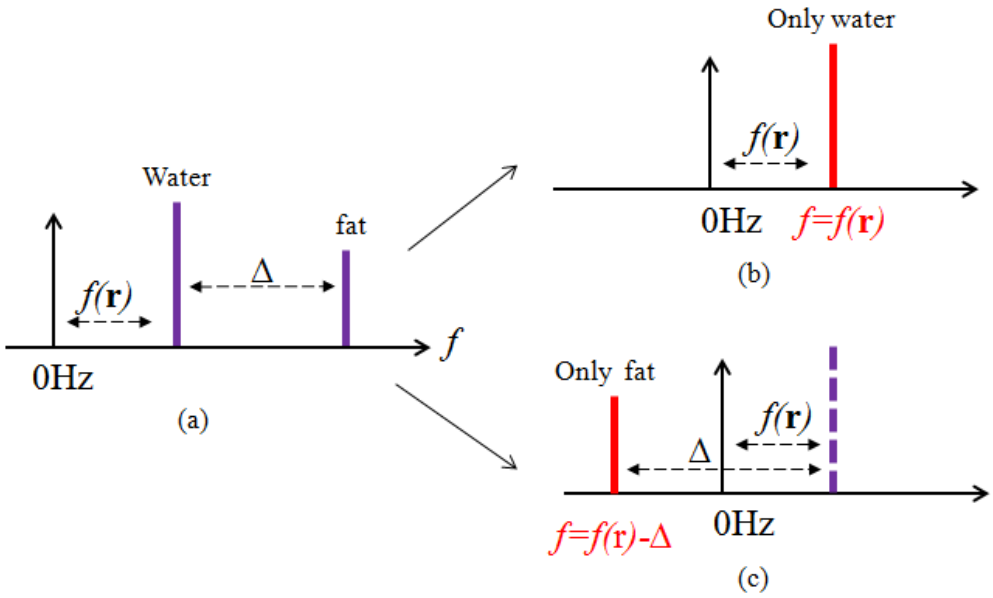

Figure 2.1: An example of ambiguity of the signal model. Suppose $f(\mathbf{r})$ is the mathematical solution of the signal model. If the pixel contains both fat and water signal, then the acutal field value $f = f(\mathbf{r})$; If there is only water signal, the actual value is still $f = f(\mathbf{r})$; If there is only fat signal, then the actual field value is $f = f(\mathbf{r}) - \Delta$. Δ is the chemical shift between water and fat in Hz. However, additional prior information is needed to determine what the composition of signal model is at the location.

In general, there are three major buckets of methods: 1) Voxel independent methods such as the initial Dixon two-point method [38], the analytical three-point technique [42] and the iterative decomposition of water and fat with echo asymmetry and least-square estimation (IDEAL) [43]. These methods generally do not utilize the assumption of field map smoothness, or consider a mild field inhomogeneity (close to 0). 2) Morphological approaches such at region growing [44, 45], region merging [46], and region based labeling [47, 48]. This type of methods usually employ the smoothness assumption as an anatomical, structural or heuristic prior in the estimation of field map. 3) Graph cut method such as [41], which models the estimation as an

www.manaraa.com

energy minization problem and solve it using an iterative graph cut algorithm. There are also many hybrid methods that combine two or more above mentioned strategies to account for the field inhomogeneity [49–52].

Voxel independent methods

In [38] 'simple proton spectroscopic imaging', Dixon proposed the two-point method, which is the first fat water separation method. The main idea is to acquire two images, one 'in-phase' when fat and water phases are aligned such as at the beginning of the spin echo $t_0 = 0$, and the other 'opposed' at the first time that fat and water have the opposite phase (t_1). Therefore, the measurement $s(t_0)$ is the summation of fat and water signals and $s(t_1)$ is the difference between water and fat:

$$\begin{aligned} s(t_0) &= \rho_{\text{water}} + \rho_{\text{fat}} \\ s(t_1) &= \rho_{\text{water}} - \rho_{\text{fat}} \end{aligned} \tag{2.3}$$

Then the water-only image is simply the addition of $s(t_0)$ and $s(t_1)$ while the fat-only image is the subtraction of $s(t_0)$ and $s(t_1)$. The problem with this method is the assumption of no field inhomogeneity present during data acquisition. Since the magnetization (phase) changes drastically between the first and second data collecting point, it is impossible to get a water and fat image by a simple addition and subtraction. An absolute value was used instead of the complex valued image data as a compensation. Further studies of two-point methods [53–55] focused on new ways of B0 inhomogeneities correction. Following the same analytical strategy, a few

www.manaraa.com

methods were later proposed to improve the original two-point method by sampling at three time points while the assumption of field variation can only be held to a restricted range [42, 56].

Both two-point and three-point methods have limitations including the restriction of two or three echo times for data collection, inability to extend the method to more metabolites and absence of large field inhomogeneity in the scheme. One way to address these limitations is to model the field map estimation in a maximum likelihood framework. Specificially, the unknown parameters in Eq.2.2 can be obtained by minimizing the least-square error between the model and the measured data [57]:

$$\{\rho_{\text{water}}, \rho_{\text{fat}}, \gamma\} = \arg \min_{\rho_{\text{water}}, \rho_{\text{fat}}, \gamma} \|\mathbf{A}_\gamma \mathbf{g} - \mathbf{s}\|^2. \tag{2.4}$$

In order to solve the above least-square error minimization problem, the iterative decomposition of water and fat with echo asymmetry and least-square estimation (IDEAL) method was proposed by Reeder *et al.* in [43]. The method solves an iterative nonlinear least-square fitting problem at each voxel. The signal model use in IDEAL is slightly different from Eq.2.1 and can be expressed as:

$$s(\mathbf{r}, t_n) = \sum_{i=1}^{M} \rho_i(\mathbf{r}) e^{j2\pi f_i(\mathbf{r})\, t_n}, \quad n = 1, \ldots, N \tag{2.5}$$

Here, the initial estimate of the field map is known and the amplitudes of metabolites are complex values. Hence, the phase term is incorporated in the amplitude ρ_j. By replacing the signal model with Eq.2.5, IDEAL solves a mamixmum likelihood

www.manaraa.com

formluation similar to Eq.2.4. IDEAL converts the nonlinear least-square problem to a series of linear estimations by iteratively solving for the incremental pertubations to the unknown parameters. The iterative process starts with an initialization of $f_i(\mathbf{r})$ and $\rho_i(\mathbf{r})$ (the real and imagery parts in actual calculation), then Eq.2.5 becomes linear and can be solved by simple matrix operations. The entire process is continued until the fitting error reaches a local convergence at this voxel.

The original IDEAL method has overcome the limitations of the two- and three-point dixon models. It can take in more than three echo time shifts and arbitrary number of metabolites in the model. It further allows complexed values in the amplitude and solves the nonlinear model with an iterative and linearized procedure. However, one main disadvantage of this method is the solution converges to local minima which often results in fat and water swaps. The maximum likelihood framework is simply a data fitting model without taking into accout the assumption of field map smoothness.

Morphological methods

In order to better account for the field inhomogeneity, an extension of IDEAL, a region growing scheme for IDEAL was proposed by Yu *et. al* in [45]. In this work, the multiecho data is firstly downsampled and an initial estimate of the low resolution field map is performed by using pixel independent fitting as in Eq.2.5. Then field map smoothness is imposed by placing a 'super-pixel' in the low resolution field map as a seed to start region growing. Berglund et. al in [44] also proposed a similar region

www.manaraa.com

growing strategy but with multiple seeds at different regions of the image.

Another morphological strategy often employed is to use multiresolutional hierarchy in hopes to guide the field map estimation [51,58]. In general, multi-resolution methods downscale the original images to a lower resolution, where analytical methods like IDEAL are performed to find out the voxel independent solution of field value at each location as a coarse estimate. Then the coarse estimate of the low resolution field map is used as a navigating map for other morphological operations such region growing [45], region merging [46] or region labeling [47] to propogate the low resolution estimate to the finer resolution.

In general, morphological methods tend to have the following characteristics:

1. Downsampling for a coarse estimate. Many methods use different downsample techniques to obtain a rough estimate of the field inhomogeneity map. The benefit of this strategy is it can provide a reliable guidance to further operations for field estimation. Some studies even design a multilayer resolution hierarchy to joint estimate the field map on the finest level, similar to the 'majority vote' idea. The computation for the entire algorithm can be saved by computing the least-square fitting error in a low resolution scale of the original data. One possible concern is low resolution estimate already exploits the field map smoothness assumption, where the field variation should be little or mild in a relatively small neighbohood. However, it might not be true if there are non-anatomical cavities in the object region, or the field strength is simply very strong. Therefore, the size of the downsampling factor coupled with the

www.manaraa.com

information of the scanned subject should be further studied.

2. Seeds planting for initialization. Seed planting is a key step in most morphological methods. The location and the number of seeds in the object depend on different factors including the structure of the object in the image, the preprocessing outcome (thresholding etc.) as well as the morphological operation after planting the seeds (e.g. region growing). Overplanting or underplanting seeds can both contribute to morphological artifacts in the results of field map estimation, resulting in fat water swaps.

3. Global convergence vs. Local convergence. For uniformly sampled data, the periodicity of the voxel independent fitting error can be significant in the correction estimation of field map. Many challenging datasets can have multiple local minima and one global minimum in period. The initialization of the field map values to start the iterative data fitting process is critical in determining whether the final convergence is to a local or global minimum.

Overall, morphological methods have proven successful in many applications. It can also face challenges with choices of downsampling factor, seeds planting and local convergence, which further requires a fair amount of hand tuning of parameters.

Graph cut methods

Iterative graph cut algorithms were later proposed in solving the field map estimation problem with improved performance [41,59]. Unlike morphological methods, [41]

www.manaraa.com

models the problem as an energy minimization formulation with an added smoothness regularization term. Following Eq.2.4, [41] first decouples the parameters using the VARPRO approach [60]. Specifically, the criterion is minimized with respect to some of the variables by assuming the others to be fixed, thus eliminating them from the optimization. Minimizing the above cost function with respect to the concentrations, assuming γ to be fixed, we obtain the optimal concentration estimates as $\mathbf{g}_{\text{opt}} = (\mathbf{A}_\gamma^T \mathbf{A}_\gamma)^{-1} \mathbf{A}_\gamma^T \mathbf{s}$. Substituting the optimal concentrations back in Eq.2.4, and solving for γ, we obtain

$$\gamma(\mathbf{r}) = \arg\min_{\gamma} \underbrace{\|\mathbf{A}_\gamma (\mathbf{A}_\gamma^T \mathbf{A}_\gamma)^{-1} \mathbf{A}_\gamma^T \mathbf{s}(\mathbf{r}) - \mathbf{s}(\mathbf{r})\|^2}_{\mathcal{C}(\mathbf{r},\gamma)} \tag{2.6}$$

One can again minimize the expression with respect to T_2^* to obtain a cost function that is only dependent on f:

$$f(\mathbf{r}) = \arg\min_{f} \quad \underbrace{\min_{T_2^*} \mathcal{C}(\mathbf{r},\gamma)}_{\mathcal{D}(\mathbf{r},f)} \tag{2.7}$$

Since the estimation of T_2^* values does not suffer from ambiguities, an exhaustive search over possible T_2^* values is used to obtain $\mathcal{D}_\mathbf{r}$ from $C_\mathbf{r}$ [60].

In order to address the sensitivity of the voxel-by-voxel optimization strategy specified by Eq.2.7 to multiple feasible solutions and phase wrapping, Hernando et al. [41] formulated the joint recovery of the field map at all the voxels as a smoothness regularized optimization scheme. The global criterion is the linear combination of the

www.manaraa.com

sum of $\mathcal{D}(\mathbf{r}, f)$ and a smoothness penalty [41]:

$$\hat{f} = \arg\min_{f(\mathbf{r})} \underbrace{\sum_{\mathbf{r}} \mathcal{D}(\mathbf{r}, f(\mathbf{r}))}_{\text{data consistency term}} + \underbrace{\mu \sum_{\mathbf{r}} \sum_{\mathbf{s}\in\mathcal{N}(\mathbf{r})} w_{\mathbf{r},\mathbf{s}} \, |f(\mathbf{r}) - f(\mathbf{s})|^2}_{\text{smoothness regularization}} . \tag{2.8}$$

Here, $\mathcal{N}(\mathbf{r})$ is the local neighborhood of the voxel at location $\mathbf{r}$ and $w_{\mathbf{r},\mathbf{s}}$ are pre-defined weights that specify the relative importance of each difference term. The first term is the sum of the voxel-independent criteria in Eq.2.7, while the second term promotes field map smoothness. Hernando et al., convert the above continuous problem to a discrete optimization scheme by restricting the field map to a set of discrete values.

The direct discrete minimization of Eq.2.8 using a graph cut algorithm is computationally infeasible, since it involves a large and fully connected graph. Hence, the authors solve it iteratively by solving a sequence of binary decision problems at each iteration; these decision problems are solved efficiently using graph cut. At the $(n+1)^{\text{th}}$ iteration, they consider two possible solutions at each voxel: $\Gamma_{n+1}(\mathbf{r}) = \{f_n(\mathbf{r}), g_n(\mathbf{r})\}$. Here, $f_n(\mathbf{r})$ is the optimal solution from the previous iteration, while $g_n(\mathbf{r})$ is chosen as $f_n(\mathbf{r}) \pm \beta$, where β is a pre-specified constant, or picked randomly a set of local minimizers of $\mathcal{D}(f(\mathbf{r}))$. Each binary decision problem is efficiently solved using graph cut and is guaranteed to converge to a global minimum. However, the iterative algorithm is still not guaranteed to converge to the global minimum of the cost function. The local minima effects sometimes manifest as fat water swaps in challenging datasets

We have so far reviewed three major classes of methods for field map estima-

www.manaraa.com

tion and fat water separation: voxel independent methods, morphological methods and graph cut methods. These methods have been validated in a wide range of applications with proven successes. Many of the problem formulations proposed in these methods have also inspired the work of this thesis and laid the foundation for some of the concepts that will appear in later sections. What has remained challenging in fat water separation are the following:

1. Large field inhomegeneity: Most of the state-of-the-art methods can obtain correct results of fat water separation in cases with reasonable field variation. However, large field variations especially within a small region of the object such as in liver or sinus can still cause iterative methods to fail due to incorrect initializations.

2. Global minima vs. Local minima: It is still a challenge to provide consistent convergence to global minima over local ones. This is particularly true for the difficult datasets such as with large field inhomegeneity . Many methods can provide global optimality in each step of a greedy strategy, but fail to guarantee a global convergence of the overall greedy strategy.

3. Computational complexity: As MRI hardware continues to develop, MRI datasets are becoming increasingly larger due to the higher resolution in all spatial dimensions and higher field strength such as 7T. This transfers into an increase of data size as an overall trend. It also can cause an increase of sheer value in the calculation of the least-square fitting model which possibly requires a large

www.manaraa.com

data storage in computation.

2.4 Graph Seach Methods

As noted earlier in Chapter 1, the terms graph search and optimal surface segmentation method are used interchangebly, due to the popularity of the former term (graph search) but both the methods refer to the same method [61].

Graph based methods have well studied in the field of computer vision [62–67]. Graph search (optimal surface segmentation) was initially published by Wu et al in [68] where a graph based framework is proposed to solve for a multiple surfaces segmentation problem. Since then graph search and its variations have been widely used in many applications, especially various medical image segmentation applications [69–82]. In general, the graph search framework transforms a discrete image/label volume into a multi-column graph space where every voxel in the original volume corresponds to a node in the graph. Nodes in the graph model are connected by various edges. The combination of nodes and edges constitute the model of the surface and possible prior constraints on graph connectivity. The purpose of the graph connectivity and constraints is that the solution of the same using a minimum *st*-cut [62] will provide the resultant surfaces.

Graph search methods [61,83] are robust schemes employed for optimal surface segmentation of multiple globally optimal surfaces in volumetric datasets. For the scope of this thesis, we will only focus on single surface segmentation/estimation. The method is characterized as a model that segments both 'terrain like' and 'closed'

www.manaraa.com

surfaces with global optimality with pre-defined constraints. Through the method is extensible to the segmentation of more complex topologies with different prior assumptions [84], we will briefly discuss the method for segmenting single terrain like surface in a 3D image volume represented as a cube.

Consider a volumetric image $I(x, y, z)$ of size $X \times Y \times Z$. A surface is defined as a function $S(x, y)$, where $x \in \mathbf{x} = \{0, 1, ...N_x - 1\}$, $y \in \mathbf{y} = \{0, 1, ...N_y - 1\}$ and $S(x, y) \in \mathbf{z} = \{0, 1, ...N_z - 1\}$. Each (x, y)-pair corresponds to a *column* of voxels $\{(I(x, y, z)|z = 0, 1, \ldots, Z - 1\}$, denoted by $col(x, y)$ parallel to the z-axis. We use $\mathbf{r}_1$ and $\mathbf{r}_2$ to denote two neighboring (x, y)-pairs in the image domain $\mathbf{x} \times \mathbf{y}$ and $N_\mathbf{r}$ to denote the neighborhood setting of image domain. The function $S(\mathbf{r})$ can be viewed as labeling for $col(\mathbf{r})$ with the label set $\mathbf{z}$ ($S(\mathbf{r}) \in \mathbf{z}$).

The method enables the incorporation of the following prior information. First, the likelihood of a voxel belonging to a given surface S where the inverse likelihood for each voxel is encoded in the graph and is termed as the data cost on each node. Second, the smoothness of a given surface S which is defined as the maximum allowed 'jump' of any two adjacent nodes on a feasible surface in a given direction ('hard constraint'). These constraints are incorporated by adding inter-column edges between nodes of a pair of neighboring columns in graph G for surface S. The surface function $S(\mathbf{r})$ intersects $col(\mathbf{r})$ at one and only one single voxel location. The objective of the method is to find a globally optimal surface $S(x, y)$ in I subjected to prior informations of node costs and certain pre-defined constraints encoded on edges. A single minimum st-cut is then computed on graph G to obtain the target surface estimation

www.manaraa.com

S.

The surface smoothness $\sum_{(\mathbf{r}_1,\mathbf{r}_2)\in N_{\mathbf{r}_1}} V_{\mathbf{r}_1\mathbf{r}_2}(S(\mathbf{r}_1), S(\mathbf{r}_2))$ as shown in Eqn 2.9, dictates the feasibilty of surface locations between two neighboring columns. The surface smoothness term then is modeled as a hard constraint and specifies the maximum possible difference between surface positions of two neighboring columns.

$$V_{\mathbf{r}_1\mathbf{r}_2}(S(\mathbf{r}_1), S(\mathbf{r}_2)) = \begin{cases} \infty, & \text{if } |S(\mathbf{r}_1) - S(\mathbf{r}_2)| > \alpha, \\ 0\ , & \text{otherwise} \end{cases} \tag{2.9}$$

where α is the hard constraint imposed for surface smoothness.

An important advantage of the graph search model is its adaptibility to the use of various cost function formulations. For example, a smoothness constrained formulation can be modeled as a graph search problem with only node costs (for data consistency error) while edge connectivity imposes the smoothness constraint. At the same time, a smoothness penalized formulation can be constructed as a graph model with both node and edge costs, where the smoothness penalty can be designed with many variations depending on applications. Alternatively, the surface smoothness $\sum_{(\mathbf{r}_1),S(\mathbf{r}_2)\in N_{\mathbf{r}_1}} V_{\mathbf{r}_1\mathbf{r}_2}(S(\mathbf{r}_1), S(\mathbf{r}_2))$ as shown in Eqn 2.10, dictates the feasibilty of surface locations between two neighboring columns. The surface smoothness term then is modelled as a 'soft constraint' and specifies the possible penalty an edge connection needs to pay between surface positions of two neighboring columns.

$$V_{\mathbf{r}_1\mathbf{r}_2}(S(\mathbf{r}_1), S(\mathbf{r}_2)) = w \times f(S(\mathbf{r}_1) - S(\mathbf{r}_2)) \tag{2.10}$$

www.manaraa.com

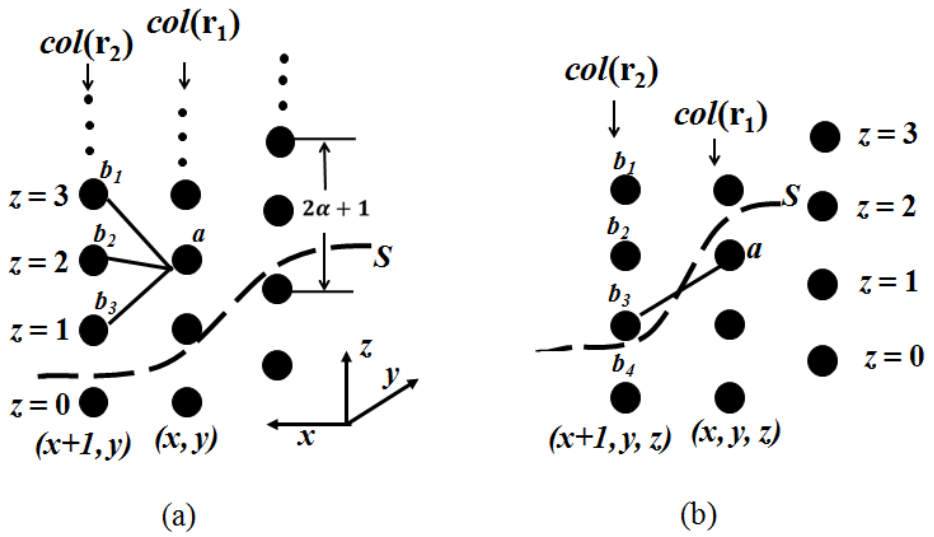

Figure 2.2: (left) Surface smoothness constraint for two neighboring columns $\mathbf{r}_1$ and $\mathbf{r}_2$ for a surface S. The arcs show the feasible st-cut for a given surface position $S(\mathbf{r}_1)$ for column $\mathbf{r}_1$. (right) Surface smoothness penalty for two neighboring columns $\mathbf{r}_1$ and $\mathbf{r}_2$ for a surface S. The arc shows a st-cut for a given surface position $S(\mathbf{r}_1)$ for column $\mathbf{r}_1$. The smoothness cost for the given cut is $w \times f(S(\mathbf{r}_1) - S(\mathbf{r}_2))$.

where $f(S(\mathbf{r}_1) - S(\mathbf{r}_2))$ is a convex function, defining the soft constraint imposed for surface smoothness. The coefficient w can be used as a tuning parameter to control the degree of regularization of the surface (provides for a balance between the data cost term and the surface smoothness term). Example of the surface smoothness and surface separation constraints are shown in Figure 2.2.

Last but not least, the graph method guarantees **global optimality** with respect to the different constraint formulations employed. This is critical because this can guarantee a constistent and reliable solution to many optimization problems where many iterative methods can only achieve local optimality.

www.manaraa.com

CHAPTER 3
FAT WATER SEPARATION USING GLOBALLY OPTIMAL SURFACE ESTIMATION (GOOSE)

3.1 Introduction

As we discussed earlier in Chapter 2, the estimation of field map inhomogeneity in the problem of fat-water decomposition is challenging especially in cases with large presence of field variations, anatonmical cavity such as in lung images, or regions of low signal to noise ratio. Traditional methods rely on voxel-by-voxel fitting of the signal model to the measured data [38, 42, 43]. The voxel-by-voxel fitting approach suffers from the non-convexity of the associated maximum likelihood criterion, which makes iterative algorithms such as iterative decomposition of water and fat with echo asymmetry and least-squares estimation (IDEAL) [43] sensitive to field map initializations. The estimation is also made difficult by the presence of phase wraps in body regions with large field inhomogeneity and ambiguities in voxels with only one metabolite (e.g. water-only voxels), which manifest as spurious fat water swaps in the decompositions.

Graph based methods have shown promising results in such cases with the idea of global optimization. For example, Hernando et al. in [41] formulated the estimation problem as the minimization of a global criterion, which is the linear combination of the sum of the voxel-independent criteria and a field map smoothness penalty, and solve it using an iterative graph cut algorithm. Specifically, a one-layer graph is constructed at each iteration; the vertices at each voxel correspond to the

www.manaraa.com

frequency value at the previous iteration and a new guess. The global optimum of this one-layer graph problem is obtained using efficient s-t cut algorithms [63, 64, 85–88]. While this iterative approach is computationally efficient, the whole algorithm is not guaranteed to converge to the global minimum of the specified cost function.

The main focus of this chapter is to introduce a novel non-iterative graph algorithm for fat water decomposition. We first formulate the recovery of the field map at all the image voxels as a constrained optimization scheme. The proposed global criterion is the sum of the voxel independent maximum likelihood criteria. While this global optimization scheme is similar to that of Hernando et al. [41], the main difference is the lack of smoothness penalty term in our global criterion. We instead rely on constraints to enforce the smoothness of the field map. Specifically, the differences in field map between adjacent voxels are constrained in a small range. The discretization of this problem yields a graph optimization problem, where each vertex of the graph is constrained to be connected with a small number of its neighbors. Thanks to the reduced connectivity, the three-dimensional graph search problem can be directly solved using an optimal surface segmentation algorithm [88] in a realistic run time. The non-iterative algorithm is guaranteed to converge to the global minimum of the constrained optimization problem.

In the following sections, we first briefly review the background of the mathematical presentation of the problem formulation. Then the smoothness constrained formulation for field map estimation is introduced. In particular, the discretization of the volumetric field map space is described for the graph construction. Next, we

www.manaraa.com

compare the proposed algorithm against several state-of-the-art fat water decomposition algorithms available in the ISMRM fat water toolbox on several challenging cases. These datasets are made available as part of the 2012 ISMRM Challenge. The qualitative and quantitative comparisons demonstrate that the proposed scheme is capable of minimizing fat water swaps in these challenging cases.

3.2 Background

We now briefly review the signal model and the problem formulation in the graph cut algorithm. In gradient echo acquisitions, the signal is collected in a succession of echo time (TE) shifts, $t_1, t_2, \ldots, t_N$. At each location $\mathbf{r} = (x, y, z)$, it can be expressed as a combination of fat and water components. The matrix form can be expressed as:

$$\underbrace{\begin{bmatrix} e^{-\gamma t_1} & e^{-\gamma t_1}\left(\sum_{i=1}^{M}\beta_i e^{j2\pi\delta_i t_1}\right) \\ .. & \\ e^{-\gamma t_n} & e^{-\gamma t_n}\left(\sum_{i=1}^{M}\beta_i e^{j2\pi\delta_i t_n}\right) \end{bmatrix}}_{\mathbf{A}_\gamma} \underbrace{\begin{bmatrix} \rho_{\text{water}} \\ \\ \rho_{\text{fat}} \end{bmatrix}}_{\mathbf{g}} = \underbrace{\begin{bmatrix} s[1] \\ .. \\ s[N] \end{bmatrix}}_{\mathbf{s}}. \tag{3.1}$$

In Eq.3.1, the model contains one water peak and **M** fat peaks, each of which has a chemical shift δ_i to the water peak. $\rho_{\text{water}}, \rho_{\text{fat}}$ are the complex valued concentrations of water and fat and β_i denotes the relative weight of each peak. $\gamma(\mathbf{r}) = [1/T_2^*(\mathbf{r}) - j2\pi f(\mathbf{r})]$, represents the combined effect of the local frequency shift $f(\mathbf{r})$ due to the static field inhomogeneity and the T_2^* decay. Assuming that β_i and δ_i are known [40], the unknowns $\rho_{\text{water}}, \rho_{\text{fat}}$ and $\gamma(\mathbf{r})$ ($f(\mathbf{r})$ and T_2^*) at each voxel can be

www.manaraa.com

obtained by minimizing the least-square error between the model and the measured data $\|\mathbf{A}_\gamma \mathbf{g} - \mathbf{s}\|^2$. The estimation of T_2^* can be achieved through an independent search over a reasonable range of discrete T_2^* values [41]. For a specific value of $f(\mathbf{r})$ and $T_2^*(\mathbf{r})$, the concentrations ρ_{water} and ρ_{fat} can be obtained as $\mathbf{g} = (\mathbf{A}_\gamma^T \mathbf{A}_\gamma)^{-1} \mathbf{A}_\gamma^T \mathbf{s}$. Substituting the optimal values for a specific frequency back, we obtain:

$$\hat{f}(\mathbf{r}) = \arg\min_{f(\mathbf{r})} \underbrace{\min_{\rho_{\text{water}}, \rho_{\text{fat}}, T_2^*} \|\mathbf{A}_\gamma \mathbf{g} - \mathbf{s}\|^2}_{\mathcal{D}(f(\mathbf{r}))} \tag{3.2}$$

Here, $\mathcal{D}\left(f(\mathbf{r})\right)$ is the voxel independent maximum likelihood prior. In order to address the sensitivity of the voxel-by-voxel optimization strategy specified by Eq.3.2 to multiple feasible solutions and phase wrapping, Hernando et al. [41] formulated the joint recovery of the field map at all the voxels as a smoothness regularized optimization scheme. The global criterion is the linear combination of the sum of $\mathcal{D}(\mathbf{r}, f)$ and a smoothness penalty [41]:

$$\hat{f} = \arg\min_{f(\mathbf{r})} \underbrace{\sum_{\mathbf{r}} \mathcal{D}(\mathbf{r}, f(\mathbf{r}))}_{\text{data consistency term}} + \underbrace{\mu \sum_{\mathbf{r}} \sum_{\mathbf{s} \in \mathcal{N}(\mathbf{r})} w_{\mathbf{r},\mathbf{s}} \left| f(\mathbf{r}) - f(\mathbf{s}) \right|^2}_{\text{smoothness regularization}}. \tag{3.3}$$

Here, $\mathcal{N}(\mathbf{r})$ is the local neighborhood of the voxel at location $\mathbf{r}$ and $w_{\mathbf{r},\mathbf{s}}$ are predefined weights that specify the relative importance of each difference term. The first term is the sum of the voxel-independent criteria in Eq.3.2, while the second term promotes field map smoothness. Hernando et al., convert the above continuous problem to a discrete optimization scheme by restricting the field map to a set of

www.manaraa.com

discrete values. At the $(n+1)^{\text{th}}$ iteration, they consider two possible solutions at each voxel: $\Gamma_{n+1}(\mathbf{r}) = \{f_n(\mathbf{r}), g_n(\mathbf{r})\}$. Here, $f_n(\mathbf{r})$ is the optimal solution from the previous iteration, while $g_n(\mathbf{r})$ is chosen as $f_n(\mathbf{r}) \pm \beta$, where β is a pre-specified constant, or picked randomly a set of local minimizers of $\mathcal{D}(f(\mathbf{r}))$. Each binary decision problem is efficiently solved using graph cut and is guaranteed to converge to a global minimum. However, the iterative algorithm is still not guaranteed to converge to the global minimum of the cost function.

3.3 Smoothness-constrained Problem Formulation

We now propose a new way to formulate the estimation of the field map $f(\mathbf{r})$ as the constrained optimization scheme:

$$\begin{aligned} \hat{f} \;=\; \arg\min_{f(\mathbf{r})} \sum_{\mathbf{r}} \mathcal{D}\left(\mathbf{r}, f(\mathbf{r})\right) \quad \text{such that} \\ |f(\mathbf{r}+\mathbf{e}_x) - f(\mathbf{r})| \le F \\ |f(\mathbf{r}+\mathbf{e}_y) - f(\mathbf{r})| \le F, \end{aligned} \tag{3.4}$$

where $\mathbf{e}_x = (1,0)$ and $\mathbf{e}_y = (0,1)$ are the unit vectors in the x and y directions, respectively. Instead of the smoothness penalty on the field map used in [41], we constrain the differences between field map values at adjacent voxels to be less than F (Hz) to minimize the ambiguities. Decreasing the maximum step size will result in a smoother field map. Note that Eq.3.4 simplifies to a fully decoupled voxel-by-voxel search when the restrictions are removed (i.e, $F = \infty$). Since the above problem is non-convex, simple gradient descent schemes are not guaranteed to converge to the

www.manaraa.com

global minimum of the criterion.

We discretize the problem by restricting the possible field map values at each location to a uniform grid specified by $f = n\,\Delta$. Here $n = -N_{\max}, ..., N_{\max} - 1$ is the discrete index and Δ(Hz) is the grid spacing. The discretization error can be controlled by setting Δ sufficiently small. The discrete optimization scheme is thus equivalent to fitting a smooth surface S to the 3-D discrete dataset $\mathcal{D}(\mathbf{r}, f)$ (see Fig. 3.1.(a)); the height of the surface at the spatial location $\mathbf{r}$ is $f(\mathbf{r})$. The number of discrete points in the surface is equal to $N_x N_y$, where the image is assumed to be of size $N_x \times N_y$. Overall, the summation in Eq.3.4] is essentially the sum of the values of the 3-D function $\mathcal{D}(\mathbf{r}, f)$ along the surface. The function $\mathcal{D}(\mathbf{r}, f)$ can be interpreted as the negative of the likelihood that the surface passes through the point $(\mathbf{r}, f)$. The likelihood of the surface is obtained by summing the likelihoods of the points on the surface.

The constraints in Eq.3.4] can be conveniently expressed by representing the discrete dataset as a connected graph $G(V, E)$ (Fig. 3.1.(b)), where V denotes the set of vertices and E are the edges. Correspondingly, the size of the graph is $N_x \times N_y \times N_f$, where $N_f = 2\,N_{\max}$ is the number of layers in the graph (the number of discrete field map values). We have one vertex for each discrete point $(\mathbf{r}, n)$, while the edges of the graph (denoted by E) are specified by the constraints in Eq.3.4. Specifically, an edge exists between the vertex $(\mathbf{r}, n)$ and $(\mathbf{r}', n')$ if and only if $|n - n'| \leq \alpha$, with α is the smoothness constraint in the graph and $\mathbf{r}$ and $\mathbf{r}'$ are neighbouring voxels; the four neighbors of the voxel $\mathbf{r}$ are $(\mathbf{r}+\mathbf{e}_x)$, $(\mathbf{r}-\mathbf{e}_x)$, $(\mathbf{r}+\mathbf{e}_y)$, and $(\mathbf{r}-\mathbf{e}_y)$. If we let R_f denote

www.manaraa.com

the complete search range of the uniform grid (Hz), then $F = \alpha\ \Delta$, $\Delta = R_f/N_f$. It can be seen that a graph surface S is a subset of V if only if it satisfies the constraints in Eq.3.4. This enables us to rewrite Eq.3.4 as

$$\hat{S} = \arg\min_{S \subset G} \underbrace{\sum_{\mathbf{v} \in V(S)} \mathcal{D}(\mathbf{v})}_{E(S)}. \tag{3.5}$$

In the above equation, $V(S)$ are the vertices of the surface. Note that each vertex is a point in 3-D: $\mathbf{v} = (\mathbf{r}, f)$. In the next subsection, we introduce the graph cut algorithm to solve Eq.3.5.

3.4 Global Optimization using Graph Search

In [89], Wu and Chen have shown that the optimal surface estimation problem can be transformed to the detection of a minimum-cost closed set in a transformed graph. A *closed set* $\mathcal{A}$ in a directed graph is a subset of graph vertices such that there is no edge from a vertex in $\mathcal{A}$ to a vertex in its complement $\mathcal{A}^c$ (Fig. 3.2.(a)). The cost of the closed set $\mathcal{A}$ is defined as the total sum of the costs of all vertices in $\mathcal{A}$. The transformation of the original problem to minimum-cost closed set enables us to solve Eq.3.5 using efficient polynomial time s-t cut schemes [90,91]. This approach is akin to transformation of a surface integral to a volume integral using Gauss theorem in the context of parametric snakes [92].

The key step in the graph transformation is the identification of a closed set $B(S)$, which has a one-to-one mapping with a surface S. For a feasible surface S,

www.manaraa.com

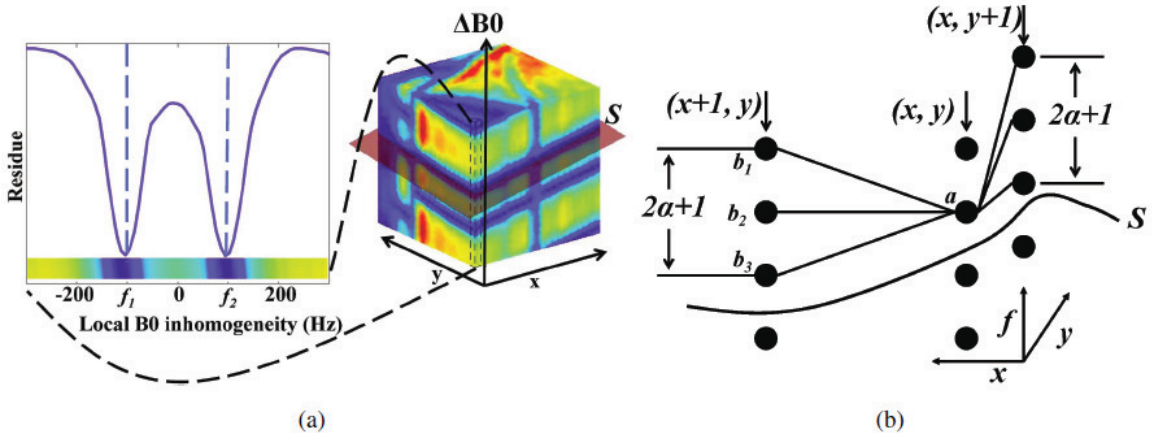

Figure 3.1: (a) Illustration of the graph cut algorithm. The residues specified by $\mathcal{D}(\mathbf{r}, f)$ are discretized on a uniform frequency grid $n\Delta; n = -N_{\max}, ..., N_{\max} - 1$. The discrete optimization is essentially a surface detection problem on a graph with $2N_{\max}$ layers, where the residues at each vertex are the vertex costs. Note that there are both local and global minimal costs in the graph. In this example the local minimal cost at f_1 are very close to the global minimal cost at f_2, for which voxel-independent schemes mostly fail. (b) Illustration of the constraints in graph-cut optimization. Each vertex on a specific voxel is connected with $(2\alpha + 1)$ neighbors. For example, the vertex a at the spatial location (x, y) is only connected with b_1, b_2, and b_3 in the column corresponding to its neighbouring voxel $(x + 1, y)$. Similarly, it is only connected to $(2\alpha+1)$ neighbors in the voxel $(x, y+1)$. S is the surface that intersects one voxel at each column within the smoothness constraint. The objective of the graph cut optimization is to search for the surface with minimal costs.

we define $B(S)$ as the set of all the vertices of G that are on or below S. It can be observed that *for any feasible surface S in G, the bottom-most neighbors of every vertex in $B(S)$ are also contained within $B(S)$*. The bottom-most neighbour of a vertex $v \in V$ is the vertex in the neighboring column with the smallest f-coordinate, which can co-exist with v on a feasible surface (See Fig. 3.2.(b)). We also transform the cost of each vertex in the graph G (denoted by $\mathcal{D}'$):

$$\mathcal{D}'(\mathbf{r}, n) = \begin{cases} \mathcal{D}(\mathbf{r}, n) & \text{if } n = -N_{\max} \\ \mathcal{D}(\mathbf{r}, n) - \mathcal{D}(\mathbf{r}, (n-1)) & \text{else.} \end{cases} \tag{3.6}$$

www.manaraa.com

Note that $\mathcal{D}'(\mathbf{r}, n)$ is essentially the derivative of $\mathcal{D}(\mathbf{r}, n)$ along the frequency direction, with the appropriate boundary conditions. We can recover the value of $\mathcal{D}$ from $\mathcal{D}'$ as $\mathcal{D}(\mathbf{r}, n) = \sum_{l=-N_{\max}}^{n} \mathcal{D}'(\mathbf{r}, n)$. Using this property [89], we can rewrite the surface sum $\sum_{\mathbf{v}\in V(T)} \mathcal{D}(\mathbf{v})$ in Eq.3.5 as

$$E(S) = \sum_{(x,y,n)\in B(S)} \mathcal{D}'(x, y, f) \tag{3.7}$$

Thus, instead of finding the optimal surface S^* directly, we seek the closed set $B(S^*)$ with the minimum cost $E(S^*)$, which uniquely defines the surface S^* . The algorithm to solve Eq.3.7 proceeds by creating a directed vertex-weighted graph $G'(V', E')$ from $G(V, E)$ [89]. The vertices $v'(x, y, f) \in G'$ has a one-to-one correspondence with the vertices $v(x, y, f)$ in G. Arcs (directed edges) are added to G' to make sure that each closed set in G' includes all the vertices associated to the corresponding surface vertices plus all the "lower" vertices in G. This is done by adding two types of arcs: intracolumn arcs and intercolumn arcs. The intracolumn arcs ensure that all vertices below a given vertex (within one column) are also included in the closed set. The intercolumn arcs ensure that the smoothness constraints are satisfied.

As an example in Fig. 3.2.(c), we will consider the added arcs for one vertex v'. It will be associated with two intracolumn arcs: one directed towards the vertex immediately below it in the column and one from the vertex immediately above it. Two intercolumn arcs will also exist for each neighbouring column in the **x**-direction (**y**-direction): one directed to the bottom-most neighbour of v' on the neighbouring

www.manaraa.com

column and one from the vertex on the neighbouring column whose bottom-most neighbour on the column of v' is vertex v'. We do not show the boundary conditions to avoid cluttering the exposition of the key ideas. An outline of the algorithm is also described in the pseudo-code below.

Algorithm 3.4.1: GRAPH SEARCH FOR OPTIMAL FIELD MAP ($\mathcal{D}(x, y, f)$)

1. Construct 3D graph $G(x, y, f)$ and assign costs $\mathcal{D}(x, y, f)$ to each node
2. Transform the surface estimation to closed set estimation: $G \rightarrow G'$
   a. Transform cost at each node to $\mathcal{D}'(x, y, f)$ using [3.6]
   b. Build intra- and inter-column edges
3. Solve for the optimal closed set using minimum s-t cut algorithm
4. Recover the optimal surface S^* and refine the solution

Once the optimal surface is determined using maximum flow/s-t cut algorithm on the transformed graph G', the solutions are refined by searching on a finer grid in the range $[f(\mathbf{r}) - \Delta, f(\mathbf{r}) + \Delta]$ (see Fig. 3.3). This search minimizes the effect of discretization. Since the search is constrained in the specified frequency range, the search is computationally inexpensive and the solution is still guaranteed to satisfy the constraints in [3.4]. We also determine the optimal R_2^* for each frequency value by an exhaustive search.

www.manaraa.com

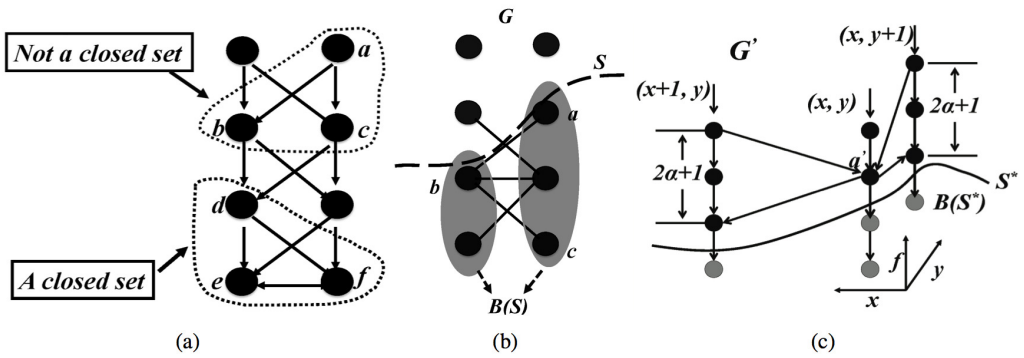

Figure 3.2: Illustration of the concepts in graph cut optimization. (a) Closed set: vertices a, b and c do not form a closed set, because vertex d which is a successor of b and c is not in the set. Nonetheless, vertices d, e and f form a closed set. (b) An example of bottom-most neighbour. Vertex a is on the surface, b is an bottom-most neighbour of a. Similarly, c is a bottom-most neighbour of b. (c) The task of finding an optimal surface S^* is transformed into finding the minimum-cost closed set $B(S^*)$ (indicated as gray vertices) beneath S^* in the directed graph G'.

3.5 3D GOOSE Formulation

Since GOOSE still processes images slice by slice, we also extend the constrained optimization scheme in GOOSE into 3D:

$$\begin{aligned} \hat{f} \;=\; \arg\min_{f(\mathbf{r})} \sum_{\mathbf{r}} \mathcal{D}\left(\mathbf{r}, f(\mathbf{r})\right) \quad \text{such that} \\ |f(\mathbf{r}+\mathbf{e}_x) - f(\mathbf{r})| \le F \\ |f(\mathbf{r}+\mathbf{e}_y) - f(\mathbf{r})| \le F \qquad (3.8) \\ |f(\mathbf{r}+\mathbf{e}_z) - f(\mathbf{r})| \le F \qquad (3.9) \end{aligned}$$

where $\mathbf{e}_x = (1,0)$, $\mathbf{e}_y = (0,1)$ and $\mathbf{e}_z = (0,1)$ are the unit vectors in the x, y and z directions, respectively. Now the smoothness constraint is applied in all three spatial dimensions. Since the graph construction and optimal surface estimation are fundamentally the same as GOOSE, we do not repeat the process here.

www.manaraa.com

3.6 Experiment Design

3.6.1 Implementation details

We use a six peak fat model, where the location of the peaks, denoted by δ_i in Eq3.1 correspond to 3.8 ppm, 3.4ppm, 2.6 ppm, 1.93 ppm, 0.39 ppm, -0.6 ppm for all the experiments. The relative weights of these peaks, denoted by β_i in Eq.3.1 are 0.0870, 0.693, 0.1280, 0.0040, 0.0390, 0.0480, respectively. These parameters are adopted from [40].

We use a discrete search procedure to determine $\mathcal{D}(\mathbf{r}, f)$ from $\mathcal{C}(\mathbf{r}, \gamma)$ according to Eq.3.2. This approach similar to the one followed in [41]. Specifically, for each value of f, we search over N_r discrete values of R_2^* in the range $0\,\mathrm{s}^{-1}$ to $500\,\mathrm{s}^{-1}$. This search process introduces minimal biases since the criterion is considerably smoother along the R_2^* dimension. We set the field map search range R_f to be [-8 ppm, 8 ppm]. Our experiments show that this search range is large enough to account for the range of field maps. The criterion specified is computed on a voxel-by-voxel basis. The optimal field map surface is then obtained by running the graph cut algorithm on the discretized problem. The discrete field map derived using the above algorithm is refined to minimize the effect of discretization. The refinement process involves an exhaustive search in the frequency range $[f(\mathbf{r}) - \Delta, f(\mathbf{r}) + \Delta]$ and the R_2^* range. The range is discretized with approximately a 1 Hz spacing and exhaustively searched to obtain the minimum. The same rule applies to the refinement of R_2^* . Finally, the fat and water volumes are estimated by solving $\mathbf{g}_{\text{opt}} = (\mathbf{A}_\gamma^T \mathbf{A}_\gamma)^{-1} \mathbf{A}_\gamma^T \mathbf{s}$; the fat volume fraction is then obtained from the derived concentrations. Since the proposed scheme

www.manaraa.com

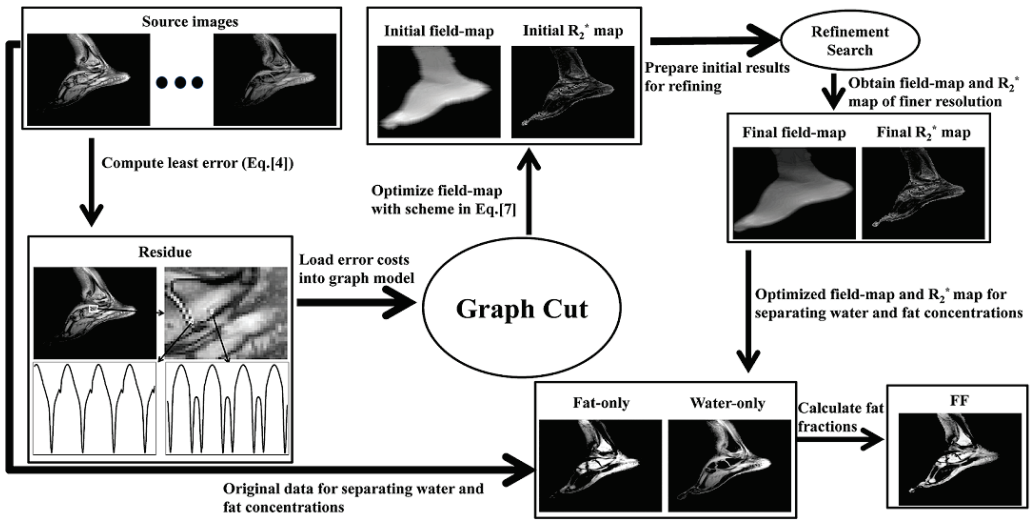

Figure 3.3: Information flow in the proposed method. The residue specified by $\mathcal{D}(\mathbf{r}, f)$ in Eq.3.2 is discretized on a uniform grid. The global optimum of the proposed constrained optimization problem is obtained using a globally optimal graph cut optimization to yield the initial field map and the initial $R_2^* = 1/T_2^*$ map. This solution is refined using a finer discrete search around the initial results provided by the graph cut algorithm. The refined field maps are used to estimate the fat water concentrations as $\mathbf{g}_{\text{opt}} = (\mathbf{A}_\gamma^T \mathbf{A}_\gamma)^{-1} \mathbf{A}_\gamma^T \mathbf{s}$.

is currently only implemented in 2D, each of the slices in multi-slice datasets are processed separately. See Fig. 3.3 for the data flow in the proposed scheme.

3.6.2 Metric used for the comparisons

We use the same metric as in 2012 ISMRM Challenge to evaluate the performance of the proposed algorithm as well as other state-of-the-art algorithms. Specifically, the performance of the algorithm is specified by the score

$$\text{Score} = \frac{\sum_{i=0}^{\text{Nvoxels}} (|\text{FF}(i) - \text{FF}_{\text{ref}}(i)| < 0.1) * P(i)}{\sum_{i=0}^{\text{Nvoxels}} P(i)} \times 100\%, \tag{3.10}$$

where FF is the fat fraction obtained from the specific algorithm and FF_{ref} is the reference fat fraction. The fat fraction is defined as the ratio of fat intensity to the

www.manaraa.com

sum of fat and water intensities. In the above equation, P is the mask, and Nvoxels is the total number of voxels. The multiplication factor is to obtain the scores in percent.

The decompositions obtained by the proposed scheme were also evaluated by an expert radiologist on a four point scale. The scales were chosen as (1): too many fat water swaps & not diagnostic quality, (2): few swaps & may be clinically misleading, (3): few swaps, but not clinically misleading, (4): no swaps & good quality.

3.6.3 Optimization of parameters

As mentioned in theory section, the proposed algorithm is dependent on three parameters:

1. N_f, the number of layers used in the graph optimization,

2. N_r, the number of discrete values of R_2^*, prior to graph optimization, and

3. α, the smoothness constraint assumed in the graph optimization; $F = \alpha * R_f / N_f$.

We determine the optimal parameters by running the proposed algorithm with different parameter choices and comparing the scores of the resulting decompositions with the reference fat water ratios on the first four datasets.

3.6.4 Comparison of algorithms

We compare the proposed scheme with the implementations of the current algorithms available in the ISMRM fat water toolbox. Specifically, comparisons are performed between the proposed method and four state-of-the-art fat water algo-

www.manaraa.com

rithms: Iterative Graph Cut Algorithm (IGCA) in [41], Safest-first Region Growing Algorithm (SRGA) in [44], Golden Section Search Algorithm (GSSA) in [45], and Hierarchial IDEAL of Multiresolution Field map (HIMF) algorithm in [52]. We assumed the default parameters provided in the toolbox for all the comparisons.

3.6.5 Datasets used for the experiments

Seventeen multi-echo datasets used in this study are distributed as part of 2012 ISMRM Challenge. The multi-slice coil-combined datasets correspond to different anatomical regions and were acquired on different institutions and different field strengths (1.5 and 3T). See Table 3.1 for details of these datasets. The reference fat-fractions and the masks corresponding to the image regions, where the fat fractions are compared, were downloaded from 2012 ISMRM Challenge website. The reference fat fractions were derived from larger number of echoes (typically 12-16 echoes) using the iterative graph cut algorithm [41]. The masks were generated by thresholding the raw images, followed by manual segmentation and binary morphological operations to exclude isolated voxels and to erode edges which are likely to be partial volume voxels. These masks were checked by an expert for validity. The number of echoes that are used for the proposed decomposition and comparison with other methods varied between the datasets, as shown by the second row in Table 3.1. All datasets were processed on a desktop computer with 3.2GHz Intel Xeon CPU and 23.6GB RAM.

www.manaraa.com

Dataset	1	2	3	4	5	6	7	8	9	10	11	12	13	14	15	16	17
# TE	6	8	5	6	4	5	6	5	6	5	6	4	4	4	4	5	3
MinTE	1.4	1.2	1.4	1.4	1.6	1.6	1.9	1.4	1.7	1.3	1.2	1.7	1.2	1.4	2.9	2.9	2.9
MaxTE	9.2	10.6	10.6	9.7	18.8	13.1	17.4	12.6	15.4	7.2	11.2	11.0	4.2	8.3	12.5	15.7	9.3
Field	3T	3T	3T	3T	1.5T	1.5T	1.5T	1.5T	3T	3T	1.5T	1.5T	3T	1.5T	1.5T	1.5T	1.5T
Anatomy	Knee	H&N	Foot	Knee	Calves	Thigh	Foot	Liver	Brain	Wrist	Liver	Liver	Thigh	H&N	Breast	Spine	Shldr
Size/x	192	225	256	192	122	122	250	224	251	192	256	157	256	256	256	160	101
Size/y	192	227	256	192	242	244	175	248	201	192	256	257	131	256	55	208	101
# Slices	4	2	2	4	5	5	5	3	3	4	5	3	4	4	5	3	4

Table 3.1: Details of the datasets used in the validation. The rows correspond to # TE: number of echoes used by the decomposition, MinTE (ms): minimum TE value, MaxTE (ms): maximum TE value, Field: field strength of the magnet, the anatomical region, Size/x: the matrix size in x, Size/y: matrix size in y, and #Slices: total number of slices in the dataset.

3.7 Results

We study the effect of the parameters N_f and N_r in Fig. 3.4.(a) and the effect of the smoothness constraint in Fig. 3.4.(c). We observe that the scores vary in a small range when $\alpha \leq 3$. The performance degrades when $\alpha > 3$. This is expected since the algorithm becomes similar to voxel-independent schemes with increasing α. Since the optimal performance is obtained at this value, we set $\alpha = 3$ in all the experiments. Specifically, the average scores from the first four datasets are obtained for different values of N_f and N_r, assuming $\alpha = 3$; the plot for different choices are shown in Fig. 3.4.(a). We observe that the algorithm is relatively insensitive to the choice of N_r, while the optimal performance is achieved around $N_f = 100$. Therefore, as we chose field map search range as [-8pm, 8pm], the grid spacing δ is approximately 10Hz for a field strength of 1.5 T and 20Hz for 3 T. Note that the constraint on the field map gets stronger as we increase N_f since F is inversely proportional to N_f. This explains why the scores drop slightly when N_f is increased beyond 100. Based on this study,

www.manaraa.com

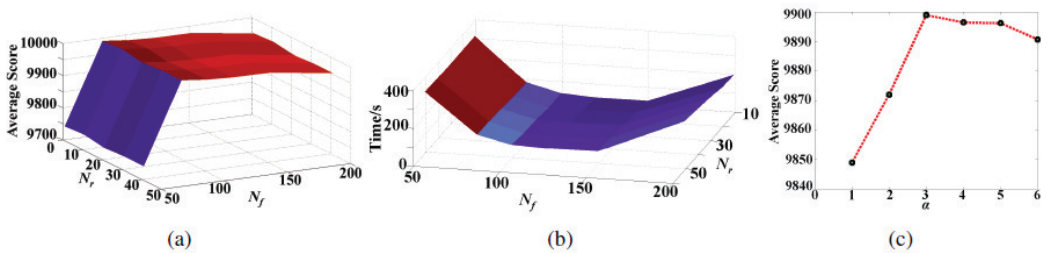

Figure 3.4: Dependence of the solution on the parameters. In (a), the number of f grid points (N_f) and R_2^* points (N_r) are varied and the resulting average scores are plotted. It is observed that the results are not too sensitive to N_r, while the best scores are obtained for $N_f \approx 100$. The average run time of the algorithms are shown in (b). For the parameters that yielded the maximum, the average run time is approximately 90 seconds. The effect of the smoothness constraints on the scores are shown in (c). Here, we assume $N_f = 100$ and $N_r = 20$. We observe that the best results are obtained when $\alpha = 3$ (i.e., 7 neighbors).

we fix $N_f = 100$ and $N_r = 20$ in the rest of the paper. Note that the computational complexity of the algorithm is dependent on N_f and N_r. The refinement is conducted in two steps: a) The field map values in the range of $[f(\mathbf{r}) - \Delta, f(\mathbf{r}) + \Delta]$ at each location are exhaustively searched with a 1 Hz resolution, assuming the R_2^* values from the first pass. b) Once the optimal frequency is determined, the R_2^* values are similarly searched exhaustively with a 1 ms^{-1} resolution. We plot the average computation time for the different choices in Fig. 3.4.(b). The average computation time for a 256x256 sized image is 90 seconds. These optimized parameters from the first four datasets are used for all the experiments. The quantitative comparisons of the GOOSE algorithm against the leading algorithms in the fat water toolbox (IGCA, SRGA, and HIMF schemes) are shown in Table 3.2. The GSSA algorithm often results in higher errors and hence were excluded from the studies. The SRGA algorithm is designed for uniformly spaced echoes and hence could not be run on dataset #3; the score is marked as N/A. The best score in each case is shown in

www.manaraa.com

Method	Mean	1	2	3	4	5	6	7	8	9	10	11	12	13	14	15	16	17
GOOSE	**99.27**	**99.84**	**99.81**	**96.50**	**99.87**	**99.94**	**99.88**	**99.90**	**99.94**	**99.97**	**99.72**	99.75	**95.58**	**99.91**	99.87	**99.15**	**99.13**	**98.80**
	3.74	**4**	**4**	3.5	**4**	**4**	**4**	**4**	**4**	**2**	**4**	**4**	1	**4**	**4**	**4**	**4**	**4**
IGCA	91.85	99.46	68.29	95.97	99.71	91.00	**99.88**	95.36	81.58	91.78	99.68	**99.91**	81.28	94.18	87.71	81.79	98.84	94.64
	2.25	**4**	1	**4**	**4**	2.5	**4**	1.5	1	1	3	**4**	1	1	1.2	1	3	1
SRGA	83.05	91.37	45.36	N/A	96.52	26.47	99.27	87.92	99.23	48.94	93.03	99.60	51.71	99.23	**99.88**	98.73	96.02	96.43
	3.06	**4**	1	N/A	**4**	1	3.5	**4**	2.5	1	**4**	3.8	1	**4**	**4**	**4**	3.2	**4**
HIMF	69.72	97.49	56.38	42.01	98.07	63.47	99.55	46.03	64.14	58.99	93.79	99.14	51.23	90.41	17.86	58.67	85.44	62.52
	2.09	**4**	1.5	1.2	**4**	**4**	2	**4**	2.1	1.8	1.5	**4**	1	1	1	1	2.5	1

Table 3.2: Quantitative comparison of the proposed scheme against state-of-the-art algorithms and qualitative evaluation by a radiologist. The first row of each algorithm indicates quantitative scores (in percent) for the 17 datasets. The second row of each algorithm indicates the average qualitative score (out of four) assigned by the radiologist. The best scores for each dataset are marked in bold. Note that SRGA works only on uniformly sampled dataset and dataset #3 is non-uniformed sampled. Therefore no score is reported from SRGA for dataset #3.

bold. It is observed that the proposed scheme provides better results in most of the challenging cases. While it provides slightly lower scores in dataset #11 and dataset #14, the scores are very close to the best performing algorithm. The qualitative scores of the decompositions obtained by the proposed algorithm by the expert radiologist are also reported in the last row of Table 3.2. The qualitative scores agreed with the quantitative scores overall. The main inconsistency was in the context of dataset #9, where the quantitative scores were high. The low qualitative scores were mainly due to the presence of small swaps in the trabecular bone regions with low signal intensity. None of the current algorithms were capable of avoiding these small swaps from limited number of echoes. The decomposition obtained from the five algorithms on a foot dataset (dataset #7) is shown in Fig. 3.5. This is a rather challenging dataset due to the large range of field inhomogeneity. It is seen that IGCA, GSSA, HIMF suffer from fat water swaps near the ankle. Similarly, GSSA and HIMF have

www.manaraa.com

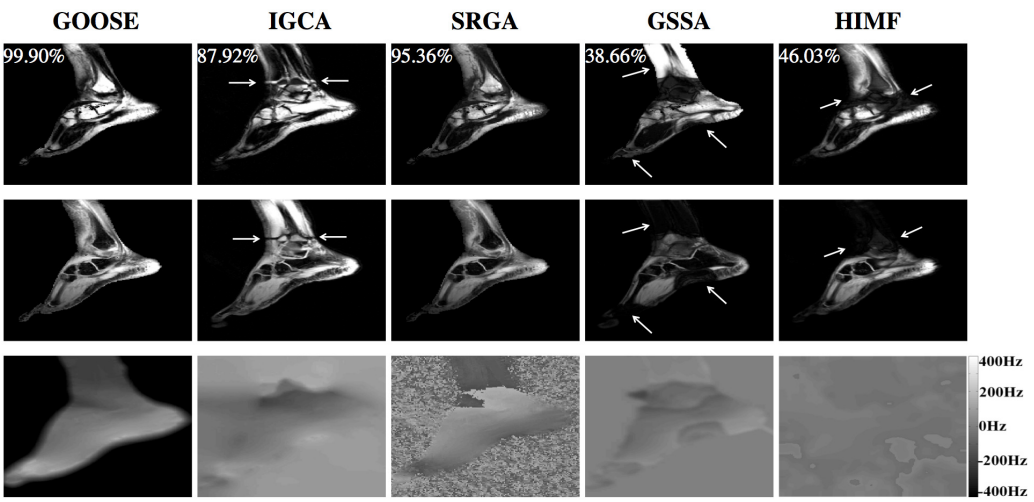

Figure 3.5: Qualitative comparisons of the algorithms on a foot dataset (2012 Challenge dataset #7). Top row: Fat; Second row: Water; Third: Field map. Fat water swaps are seen in IGCA, GSSA and HIMF indicated by arrows. The proposed and SRGA scheme are seen to provide good decompositions, which is also evident from the quantitative scores in Table 3.2 (also shown at the top left corner of each fat image).

more swaps on both leg and toe region. The field maps derived by these algorithms (see bottom row) exhibit abrupt variations indicating convergence to local minima. We observe that the SRGA algorithm, as well as the proposed scheme, is capable of providing good estimates in this example. A noticeable difference in the field map recovered by the proposed scheme is that it takes small values outside the anatomical region. This can be attributed to the constrained formulation [3.4]. Specifically, the data-consistency term $\mathcal{D}(\mathbf{r}, f)$ is considerably smaller in amplitude in regions with low signal than regions with signal. Hence, many different values of f may give the same cost. The constrained formulation will pick one solution among the possible ones that satisfy the constraints. Due to the transformation [3.6], the solutions at these voxels often correspond the first few nodes at these voxels. Another example,

www.manaraa.com

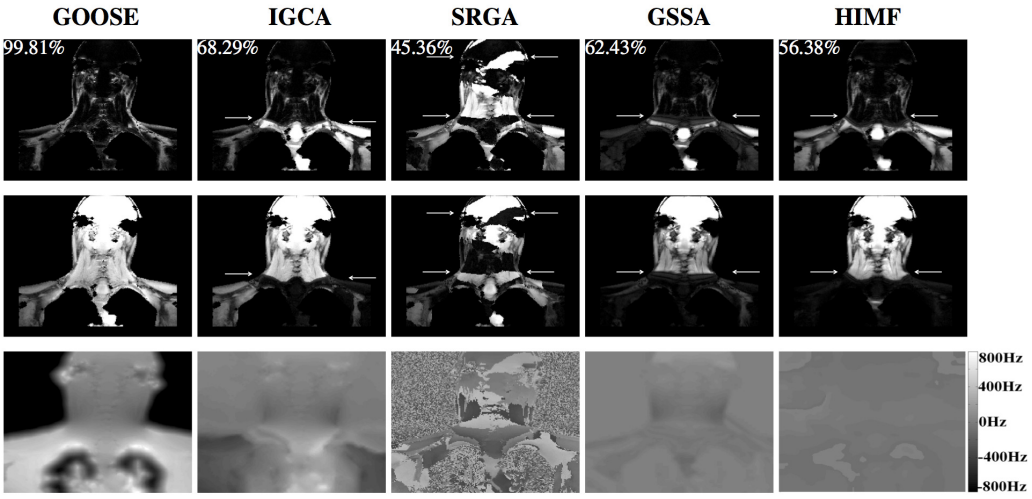

Figure 3.6: Qualitative comparisons on a head and neck dataset (2012 ISMRM Challenge dataset #2). Top row: Fat; Second row: Water; Third: Field map. All of the algorithms except the GOOSE scheme result in swaps between water and fat. Quantitative comparison can be seen from Table 3.2 (also shown at the top left corner of each fat image).

corresponding to the head/neck and upper thorax dataset (dataset #2) is shown in Fig. 3.6. This set is challenging due to the larger magnetic field inhomogeneity and multiple disconnected regions. From Fig. 3.6, we observe that all algorithms, except the proposed method, suffers from multiple fat water swaps in the region under neck. The failure of the SRGA scheme, which performed well in the other datasets, may be due to the disconnected nature of the regions and the large dynamic range; these challenges probably make the accurate seed placement in the region-growing algorithm difficult.

Fig. 3.7 shows the decomposition on an axial liver dataset (dataset #12). We observe that the existing schemes result in swaps in all the three slices, while the proposed scheme correctly recovered the fat and water in slices 1 & 3. The GOOSE algorithm also failed in slice 2, resulting in a swap. The main reason for the failure of

www.manaraa.com

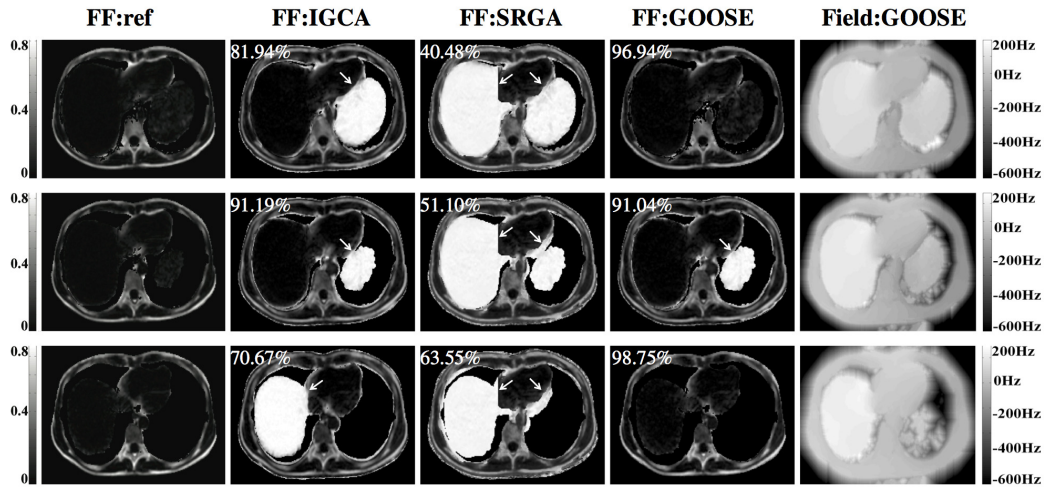

Figure 3.7: Comparison of the algorithms on 2012 ISMRM Challenge dataset #12. First column: Fat Fraction (FF) map for reference from 2012 ISMRM Challenge committee; Second: FF from SRGA; Third: FF from IGCA; Fourth: FF from GOOSE; Fifth: Field map from GOOSE. Each row corresponds to one slice in the dataset. This is a challenging example due to the disconnected regions in the dataset. We observe that all algorithms except the proposed one result in swaps in all the slices. The proposed scheme is capable of recovering the fractions correctly in slices 1 & 3 (first and third row), while it results in a swap in the second slice.

the GOOSE algorithm in this case is that the anatomical regions are disconnected; the algorithm is not able to propagate the correct solution to the region of failure. This is a fundamental problem associated with algorithms that exploit field map smoothness.

Fig. 3.8 shows the fat water decomposition of two slices of a breast dataset (dataset #15). The IGCA scheme resulted in large and obvious swaps, while the SRGA method resulted in subtle swaps, indicated by arrows. The GOOSE scheme is capable of providing results that are in good agreement with the ground truth in most regions. It resulted in a small swap in the middle, which is also indicated by arrows. In addition, the proposed 3D-GOOSE method employs a three-dimensional graph search scheme that also takes into account the field map smoothness across

www.manaraa.com

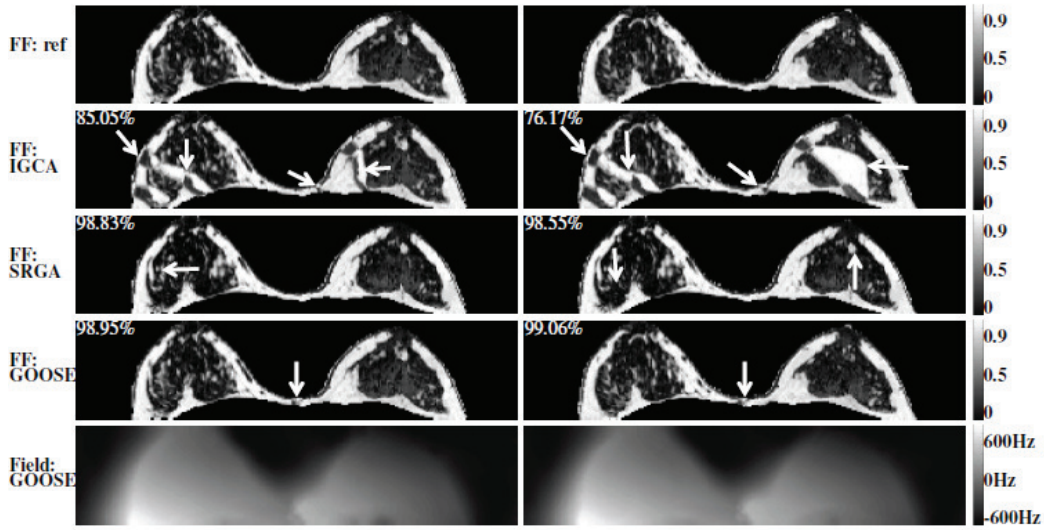

Figure 3.8: Comparison of the algorithms on a breast dataset (2012 ISMRM Challenge dataset #15). First row: Fat Fraction (FF) map for reference from 2012 ISMRM Challenge committee; Second: FF from IGCA; Third: FF from SRGA; Fourth: FF from GOOSE; Fifth: Field map from GOOSE. Each column corresponds to one slice in the dataset. IGCA results in large and obvious swaps. In contrast, the SRGA scheme results in several subtle swaps pointed by arrows.

slices. For example, we were not able to correct a small fat-water swap in one slice of the above breast dataset in GOOSE, whereas the separation is correct on all slices using 3D-GOOSE. Results can be seen in Fig. 3.9.

3.8 Discussion

We introduced a novel fat water decomposition scheme, which we term as globally optimal surface estimation (GOOSE) algorithm. The proposed algorithm uses explicit constraints to exploit the smoothness of the field map, thus minimizing the ambiguities in maximum likelihood estimation. Specifically, the differences in the field map between adjacent voxels are constrained to be within a small range (less than 25Hz). The discretization of the criterion yields a problem that can be efficiently solved using graph cut optimization. Thanks to the considerably reduced graph

www.manaraa.com

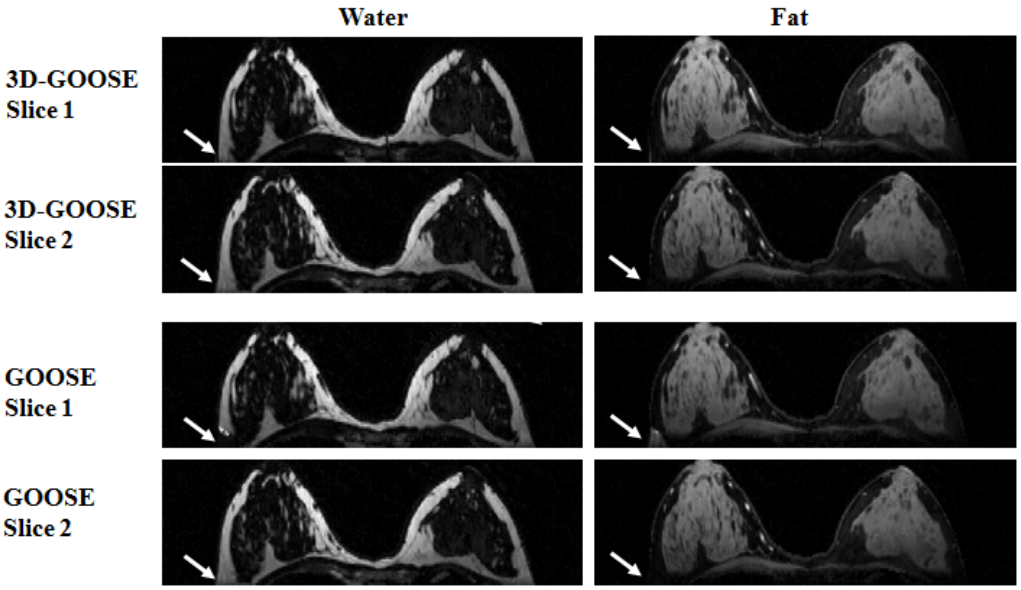

Figure 3.9: Comparison of the GOOSE and 3D-GOOSE on a breast dataset (2012 ISMRM Challenge dataset #15). In contrast, the small fat water swap scheme in GOOSE is corrected by 3D-GOOSE pointed by arrows.

connectivity, the algorithm is guaranteed to yield the global minimum of the cost function in a short computation time. While the algorithm shares some similarities with the global optimization scheme of Hernando et al. [41], the key difference is the constrained formulation. The global optimality guarantees of the algorithm are seen to be beneficial in practical settings. We have compared the proposed algorithm against some of the algorithms available in the ISMRM fat water toolbox. Overall, the comparisons show that the proposed scheme yields fewer swaps and thus better fat water decompositions. The algorithm is also evaluated independently by the 2012 ISMRM challenge committee; the decompositions using the GOOSE scheme resulted in scores that were only 0.04% lower than the winning team [93], which combined the results of several decomposition schemes in the ISMRM fat water toolbox using a perceptual quality metric [93] . While the proposed scheme may be improved

www.manaraa.com

by combining it with other methods in a similar fashion, the resulting performance improvement is not expected to be significant.

A major limitation of the proposed implementation is that it is restricted to two dimensions. Currently, the different slices in multi-slice datasets are processed independently without considering the field map smoothness across slices. The extension of this algorithm to three dimensions can provide further improvement in performance of the current two-dimensional method. Specifically, the smoothness of the field map between the slices can enable us to resolve the ambiguities in datasets with disconnected regions. For example, we anticipate that this extension will improve the performance in the context of dataset #12 (see Fig. 3.7). Specifically, the 2-D scheme recovers the first and third slices accurately, while the second slice had a swap due to the disconnected regions. This will be part of our future work.

We have adopted the fat water model in Eq.3.1, which is relatively established in the fat water community. Hence, our algorithm shares the benefits and drawbacks associated with the specific model. For example, the proposed algorithm is dependent on the number of fat peaks and their relative strengths in the model. This assumption considerably reduces the unknowns and offers a proportional reduction in variance. However, it is likely to result in biases when the relative strengths differ from actual values. Similarly, we have consolidated the decay parameters of fat and water into a single term. While the consolidation of the decay terms of fat and water into a single T_2^* term is shown to be beneficial [40, 41], this approach may introduce biases in regions where this assumption is violated.

www.manaraa.com

3.9 Conclusion

The focus of this chapter was on the development of a novel graph surface estimation method for field map estimation in MRI fat-water decomposition. In this work, a new smoothness constrained formulation was proposed to implicitly incorporate the assumption of field map smoothness. A discretized field map volume was designed for the purpose of globally optimal surface estimation. The method was developed, applied to various datasets and demonstrated the superior performance of the developed method in terms of both qualitative and quantitative accuracy metrics. The results also demonstrate that the developed method is also more efficient than the previous graph cut methods. The results clearly show the improved performance of the proposed approach and applicability in future studies and clinical applications.

www.manaraa.com

CHAPTER 4
FAT WATER DECOMPOSITION USING RAPID GLOBALLY SURFACE ESTIMATION (R-GOOSE)

4.1 Introduction

In Chapter 3, we introduced a non-iterative single-step graph search algorithm termed as GOOSE to solve a constrained optimization problem [94]. The 3D extension of GOOSE was also introduced to improve the performance by exploiting the cross-slice field smoothness and jointly processing three dimensional datasets.

In short, GOOSE and 3D-GOOSE minimize the discrete approximation of the original problem, subject to smoothness constraints on the field map. The field inhomogeneity induced frequency shifts at each pixel are assumed to be on a uniform grid. The algorithm constructs a graph with as many layers as the size of the discrete grid, where each node (corresponding to a specific pixel and frequency) in the graph is connected to only a few of the nodes in the adjacent pixel within a small range of frequencies. This constrained optimization problem is then solved using a graph search framework. The hall-mark of the algorithm is its ability to converge to the global minimum of the optimization problem as shown in [89]. The global convergence of the algorithm translates to greatly improved results over state-of-the-art methods. The ability of GOOSE to considerably reduce the swaps in challenging applications, compared to the iterative graph cut solution is seen from the experiments in Chapter 3.

Despite the improved results offered by GOOSE, the main problem associated

www.manaraa.com

with this scheme is its high computational complexity, which limits its applicability to large scale 3D problems. In particular, the complexity of the algorithm is dependent on the size of the graph, which in turn is dependent on the discretization of the field map. Typically, the problem discretization results in graphs with more than 100 layers, which are computationally expensive and memory demanding.

The main focus of this chapter is to introduce a new graph search model for fat-water decomposition that inherits the global optimality of GOOSE, while reducing the computational complexity by an order of magnitude. Here, we consider a smoothness penalized likelihood scheme, as opposed to the smoothness constrained setting in GOOSE. In particular, we formulate the field map estimation as a 3D optimization problem, where the proposed global criterion is the sum of the voxel independent maximum likelihood measurement and a smoothness regularization penalty term. Apart from the differences in the formulations, the main difference from GOOSE is the significantly smaller size of the graph. We perform a fast discrete pixel-by-pixel search to identify the local minima of the voxel independent likelihood measure at each pixel, then the solutions at each pixel are constrained in a set of local minima.

The rest of this chapter is organized as follows: We will introduce the 3D smoothness regularized formulation and illustrate the key differences from the previous smoothness constrained formulation in GOOSE and 3D-GOOSE. Then we will propose a new non-equidistant graph model to solve the smoothness regularized formulation. Finally, the comparison between GOOSE and the new algorithm, which is termed as rapid GOOSE (R-GOOSE) on the 2012 ISMRM Challenge datasets will

www.manaraa.com

be shown with further discussions on the main characteristics of the new algorithm.

4.2 Problem Formulation

4.2.1 Background

Here, we briefly review the GOOSE formulation. In GOOSE, the recovery of the field map at all pixels was formulated as a single optimization problem [94]:

$$\begin{aligned} \hat{f} \;=\; \arg\min_{f(\mathbf{r})} \sum_{\mathbf{r}} \mathcal{D}\left(f(\mathbf{r})\right) \quad \text{such that} \\ |f(\mathbf{r}+\mathbf{e}_x) - f(\mathbf{r})| \leq F \\ |f(\mathbf{r}+\mathbf{e}_y) - f(\mathbf{r})| \leq F, \end{aligned} \tag{4.1}$$

Here, $\mathbf{e}_x = (1,0,0)$ and $\mathbf{e}_y = (0,1,0)$ are the unit vectors in the x and y directions. Since $\mathcal{D}\left(f(\mathbf{r})\right)$, the voxel independent maximum likelihood prior has multiple local minima at each location, GOOSE imposes hard constraints for the permissible deviation of frequency values between adjacent voxels. To solve the above optimization problem, the frequency values are discretized onto a uniformly full grid with a grid spacing Δ, where F is assumed to be a multiple of Δ. A brief graph illustration can be seen in Fig. 4.1.(a). The readers are referred to Chapter 3 for more details.

4.2.2 Rapid Globally Optimal Surface Estimation (R-GOOSE)

We reformulate the GOOSE formulation with the focus on significantly reducing the number of layers in the graph, which will result in reduced computational complexity. Rather than considering the uniform discretization of the frequency axis,

www.manaraa.com

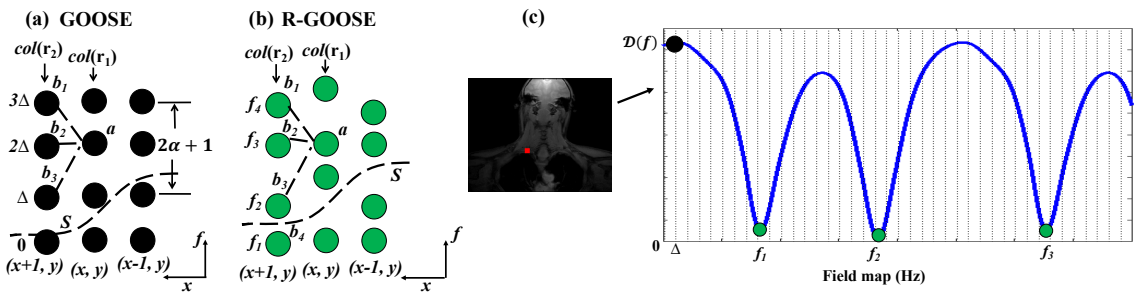

Figure 4.1: Illustration of the graph constructions in GOOSE (a) and R-GOOSE (b). For simplicity, we restrict our attention to 2-D graphs, while our implementation is in 4-D. The maximum likelihood measurement specified by $\mathcal{D}(f(\mathbf{r}))$ is discretized on a uniform grid of field map values; the plot of $\mathcal{D}(f(\mathbf{r}))$ at a specific pixel is shown in (c). (a) In GOOSE, the fieldmap was uniformly discretized with each node corresponding to a discrete frequency, indicated by the black dotted lines in (c) and the black circles in (a) and (c). A graph smoothness constraint was used in GOOSE, where each node is connected to only $(2\alpha+1)$ nearby nodes in the adjacent pixels. Here, the smoothness constraint α was 1. The node costs were chosen as $\mathcal{D}(f(\mathbf{r}))$, while no smoothness costs were considered. (b) In R-GOOSE, we only consider the local minimizers of $\mathcal{D}(f(\mathbf{r}))$, which correspond to the nodes at each pixel, indicated by the green circles in (b) and (c). Note that the nodes are not equispaced in the R-GOOSE setting. We use a graph ssmoothness penalty in R-GOOSE as opposed to the smoothness constraint in GOOSE. Hence, each node in a pixel is connected to all the nodes in the adjacent pixels. The node costs are still chosen as $\mathcal{D}(f(\mathbf{r}))$, while the smoothness cost between the i^{th} node in pixel $\mathbf{r}$ and the j^{th} node in its neighboring pixel $\mathbf{s}$ are chosen as $w_{\mathbf{r},\mathbf{s}}|f_i - f_j|^2$.The objective here is to find the surface (S) that minimizes the total of both costs.

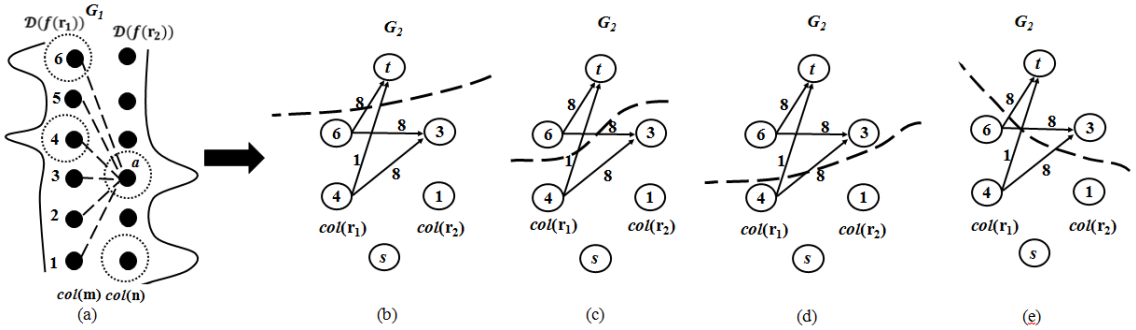

Figure 4.2: (a)-(e) An example of inter-column edge connectivity. Minimizers $col(\mathbf{r}_1) = 4, 6$ and $col(\mathbf{r}_2) = 1, 3$ are chosen to form the new graph.There are four possibilities of where the surface cuts through, indicating four combinations of minimizers in the final solution, which depends on the total cost from the combination of edges and nodes.

www.manaraa.com

we will now consider non-uniform discretization. In particular, we will choose the permissible frequency values at each pixel as the local minima of $\mathcal{D}(f(\mathbf{r}))$.

We determine the set of local minima at the spatial location $\mathbf{r}$, denoted by $\mathrm{LM}(\mathbf{r})$, by searching the finite differences of $\mathcal{D}(f(\mathbf{r}))$. Suppose at location $\mathbf{r}$, f_1, f_2 and f_3 are three consecutive field map values in the grid. We compute the finite differences $d(f_2) = \mathcal{D}(f_2) - \mathcal{D}(f_1)$, and $d(f_3) = \mathcal{D}(f_3) - \mathcal{D}(f_2)$ respectively. If $d(f_2) < 0$ and $d(f_3) > 0$, then f_2 is a minimizer. Due to the fineness of the grid in discretization, it is possible that $d(f_2) = 0$, then we continue to calculate $d(f_3)$, if $d(f_3) > 0$, then both f_2 and f_3 are minimizers. We observe that this pixel by pixel search is very fast.

Once the sets $\mathrm{LM}(\mathbf{r})$ are determined, we pose the field map estimation problem as the smoothness penalized 3D optimization problem:

$$\hat{f} = \arg\min_{f(\mathbf{r})} \sum_{\mathbf{r}} \left(\underbrace{\mathcal{D}(f(\mathbf{r}))}_{\text{data consistency}} + \mu \underbrace{\sum_{\mathbf{s}\in\mathcal{N}(\mathbf{r})} w_{\mathbf{rs}} |f(\mathbf{r}) - f(\mathbf{s})|^2}_{\text{smoothness regularization}} \right), \quad f(\mathbf{r}) \in \mathrm{LM}(\mathbf{r}); \forall \mathbf{r} \quad (4.2)$$

Here, $\mathbf{r} = (x, y, z)$, with the third dimension z as the zth slice of the image data. $\mathcal{N}(\mathbf{r})$ is the local neighborhood of the voxel at location $\mathbf{r}$ and $\mu_{\mathbf{rs}}$ are pre-defined weights that penalize the differences of the field map values in the neighborhood $\mathcal{N}(\mathbf{r})$. The first term is the sum of the voxel-independent criteria in [6] that promotes the consistency between the data model and measurements. The second term is the smoothness regularization that encourages field map smoothness. μ is the regularization parameter that balances the first term and second term. The choices

www.manaraa.com

of $f(\mathbf{r})$ are limited to LM($\mathbf{r}$), the set of minimizers at location $\mathbf{r}$. The objective of the formulation is to find out the optimal field maps in all three dimensions that minimize the sum of data consistency and field map smoothness penalty.

Similar to GOOSE, we transform the optimization problem into a graph based surface estimation problem. Herein, each element in LM(r) is represented as a node in the graph. Similarly, we denote the uniform grid is of size $N_x \times N_y \times N_z \times N_f$. N_x, N_y and N_z are the size in x-, y- and z- directions, and N_f is the number of discrete frequency values at each location (x, y, z). Let $col(x, y, z)$ represent a node column wherein $col(x, y, z) \in \text{LM}(x, y, z)$, $x \in \{0, 1.. \ldots N_x - 1\}$, $y \in \{0, 1.. \ldots N_y - 1\}$ and $z \in \{0, 1.. \ldots N_z - 1\}$. Compared to GOOSE, the nodes in the new graph are no longer equidistantly spaced. The goal of the surface estimation problem is to find a surface $S(x, y, z) = \hat{f}(x, y, z)$, such that the the surface $S(x, y, z)$ intersects each node column exactly once and the objective function shown in Eq.(5.2) is minimized.

Note the size of the sets LM($\mathbf{r}$), and hence the number of layers in graph, are considerably smaller than the size of discretized nodes in the GOOSE setting. For example, in Fig.4.1.(c), the full field map range R_f is about 0-1200Hz, therefore the graph in GOOSE contains 100 layers with a grid spacing of 12Hz. But the proposed formulation only needs to consider the three local minimizers. It is possible that the discretized nodes are not the exact local minimizers in GOOSE (maybe close neighbors of local minimizers). The new graph construction with the non-uniform discretization strategy effectively mitigates this discretization error while also reducing the computational complexity present in GOOSE formulation.

www.manaraa.com

In particular, the entries of the set LM($\mathbf{r}$) can be determined with arbitrary accuracy, while the computational complexity of the graph search algorithm depends on the number of entries in the set LM($\mathbf{r}$). The non-uniform spacing between the nodes makes it difficult to solve using conventional algorithms, which are designed for uniform sampling. We use the graph construction introduced in [95] which is briefly discussed in the next subsection to solve the optimization problem with non-uniform spacing. Since the smoothness penalty involves a convex (quadratic in our setting) distance measure, the graph algorithm [95] is guaranteed to converge to the global minimum of Eq.(5.2).

4.3 Graph Construction

Overall, the graph construction has four main steps: 1) Extract the local minimizers (LM(x, y, z)) of $\mathcal{D}(f(x, y, z),$ 2) Construct a subgraph G_z for each slice z where $z \in \{0, 1, ..N_z - 1\}$, 3) Add the intra-column and inter-column edges in G_z to encode the data consistency term and smoothness regularization term (in x and y directions) for each slice z, 4) Construct the main graph G through the union of the subgraphs G_z by adding edges between successive G_z's to incorporate the smoothness regularization term in the z direction.

The local minimizer set LM(x, y, z) is extracted by using the finite difference method at each location as discussed in the previous section. Then a subgraph G_z is constructed for each slice z where $z \in \{0, 1, ..N_z - 1\}$. Herein, each element in the set LM(x, y, z) where $x \in \{0, 1, ..N_x - 1\}$ and $y \in \{0, 1, ..N_y - 1\}$ is represented as a

www.manaraa.com

node in the graph G_z. Denote N_f as the size of $\mathrm{LM}(x, y, z)$. Thus, a subgraph G_z has $N_x \times N_y \times N_f$ nodes. Denote a column $col(x, y, z)$ for slice z where $x \in \{0, 1 \ldots N_x - 1\}$, $y \in \{0, 1 \ldots N_y - 1\}$ and $col(x, y, z) \in \mathrm{LM}(x, y, z)$. For the ease of notation denote r_1 as (x, y, z) tuple for z-th slice and r_2 as a neighboring tuple to r_1 in the z-th slice. We use 4-connectivity of graph neighborhood in x- and y- directions in this paper. At each slice z, we compute $\mathcal{D}(f(x, y, z))$ on a fine frequency grid, followed by the extraction of the local minimizers such as f_1 and f_2 in Fig.4.1.(b).

The intra-column edges are added to encode the corresponding data consistency term. Next inter-column edges are added between two neighboring columns $col(\mathbf{r}_1)$ and $col(\mathbf{r}_2)$ to encode the smoothness regularization term in the x and y directions. Details regarding the edge construction can be found in [95]. Our proposed approach uses a new graph construction which provides two major differences: 1) The graph is able to incorporate the non-equidistant nodes in a column as required due to the extraction of minimizers. 2) The graph applies a convex regularization between solutions for two neighboring columns. In other words, using the proposed approach, for a solution $S(\mathbf{r}_1) = a$, the feasible solutions for $S(\mathbf{r}_2) = b_i$ where $i \in \{0, 1, \ldots \ldots \mathrm{LM}(\mathbf{r}_2) - 1\}$, thus allowing a to talk to all the nodes in $col(\mathbf{r}_2)$ as can be seen in Fig.3.1.(d). The inter-column edges are added in a way that based on the new graph construction [95], for a given solution $S(\mathbf{r}_1) = a$ and $S(\mathbf{r}_2) = b_i$, the regularization cost is $\mu|S(\mathbf{r}_1) - S(\mathbf{r}_2)|^2$, which is the exact quadratic penalty in Eq.(5.2). It should also be noted that some of the edge weights in the new graph may be 0 and thus only positive edge weights are added.

www.manaraa.com

Next, graph G is constructed by adding inter-column edges in a similar fashion between the corresponding columns in successive subgraphs G_z and G_{z+1} to incorporate the smoothness regularization term in the z direction. Denote $\mathbf{r}_1$ as a (x, y, z) tuple for z-th slice and $\mathbf{r}_3$ as the corresponding tuple $(x, y, z+1)$ to r_1 in the $z+1$-th slice. The edge connection betweeen corresponding columns $col(\mathbf{r}_1)$ and $col(\mathbf{r}_3)$ is built in the same manner as columns $col(\mathbf{r}_1)$ and $col(\mathbf{r}_2)$, which can be seen in Fig.4.1.(b). Thus, there is a stark difference between our proposed method and the constrained graph construction in GOOSE, where for a resultant solution of $S(\mathbf{r}_1) = a$, the only feasible solutions (nodes that a can talk to) for $S(\mathbf{r}_2)$ are b_1, b_2 and b_3, by virtue of the hard constraints used in GOOSE which can be seen in Fig.4.1.(b).

Fig.4.2(a) - (e) are an example of the edge connectivity in the new graph construction. Denote a 2 by 6 graph G_1 with data consistency shown as $\mathcal{D}(f(\mathbf{r}_1))$ and $\mathcal{D}(f(\mathbf{r}_2))$ for two neighboring columns $col(\mathbf{r}_1)$ and $col(\mathbf{r}_2)$, respectively. As shown in Fig.4.2(a), $\mathcal{D}(f(\mathbf{r}_1))$ reaches the minimum when $col(\mathbf{r}_1) = 6$ and $col(\mathbf{r}_1) = 4$. Therefore we extract minimizers $col(\mathbf{r}_1) = 6$ and $col(\mathbf{r}_1) = 4$ from the uniform grid and similarly $col(\mathbf{r}_2) = 3$ and $col(\mathbf{r}_2) = 1$ to form the new graph G_2 with source s and terminal t for graph search. Based on the conditions in [95], we build four directed edges $E(6, t)$, $E(6, 3)$, $E(4, t)$, $E(4, 3)$ in the graph as shown in Fig.4.2(b) - (e). For instance, if the surface goes through $col(\mathbf{r}_1) = 6$ and $col(\mathbf{r}_1) = 3$ in Fig.4.2(b), then the total cost that surface incurs is $E(6, t) + E(6, t) = 9$, which is equal to the quadratic difference between $col(\mathbf{r}_1) = 6$ and $col(\mathbf{r}_2) = 3$. In (h), there is no directed edge between $col(\mathbf{r}_1) = 4$ and $col(\mathbf{r}_2) = 1$ but the crosstalk between these two is

www.manaraa.com

still allowed with the associated edge cost as the sum of $E(4,t)$ and $E(4,3)$. This principle also applies to Fig.4.2(c) and (e). Note that in Fig.4.2(c), the total edge cost is $E(4,t)=1$ instead of $E(t,1)+E(6,3)=9$ because only costs of edges directed from source set to terminal set are considered in calculating the max flow [89]. Here, we did not show the intra-column edges to avoid obscuring the main idea.

In GOOSE, edge connectivity between nodes has no direct contribution to the total cost. In other words, the total cost in GOOSE is only the sum of node costs $\mathcal{D}(f(\mathbf{r}))$. The objective in GOOSE is to search for an optimal surface S that intersects a set of nodes that provides the minimal total cost. However, the purpose of building the new graph is to find a set of surfaces, where each one goes through a local graph and they collectively provide the minimized combination of node and edge costs in G. A pseudo-code for the new graph construction and optimal surface search is shown below.

Algorithm 4.3.1: Graph Search for Optimal Field Map ($\mathcal{D}(f(\mathbf{r}))$)

1. Discretize field map in search range R_f
2. Extract the set of minimizers LM($\mathbf{r}$) from all locations
3. Construct graph $G(f(\mathbf{r}))$ and assign costs $\mathcal{D}(f(\mathbf{r}))$ to each node
4. Build intra- and inter-column edges with weights for smoothness penalty
5. Solve for the surface estimation using minimum s-t cut algorithm
6. Recover the optimal surfaces and refine the solution

www.manaraa.com

4.4 Experiment Design

In this work, results of the 17 datasets from 2012 ISMRM Challenge by applying the R-GOOSE framework are compared against those from GOOSE in quantitative accuracy and computation time. The quantitative accuracy, or the score is determined by the percentage of pixels in the pre-defined mask in which the difference of fat fraction between the tested result and the reference is less than a threshold (0.1). Details can be found in Chapter 3, Experiment Design section. We adopt the parameters of the reference signal model in the judging section of the 2012 ISMRM Challenge. Specifically, we use six fat spectral peaks at δ_i = [-242.7060, -217.1580, -166.0620, -123.9078, -24.9093, 38.3220] Hz at 1.5T, with relative weights β_i = [0.0870, 0.6930, 0.1280, 0.0040, 0.0390, 0.0480]. A single T_2^* constant is used at each voxel. The search of $1/T_2^* = R_2^*$ is separated as a preprocessing step before field map estimation, and is repeated with the obtained field map after graph search for optimization. Implementation details from data input, graph search to the final output of separate fat and water images can be seen in Fig.4.3.

Three parameters need to be optimized in the proposed algorithm: 1) N_f, the number of graph layers, or the number of entries in LM. N_f is expected to be able to cover the field inhomogeneity range which can be estimated by $1/\Delta$TE for uniformly sampled data. $\mathcal{D}(f(\mathbf{r}))$ is periodic and contains at least two minimizers in each period in a typical case with both fat and water for the pixel. The largest range of field inhomogeneity for all the 17 datasets is about $[0, 1020]$Hz in dataset 12 and contains up to 5 periods (about 12 minimizers). Therefore, we test $N_f = 3$

www.manaraa.com

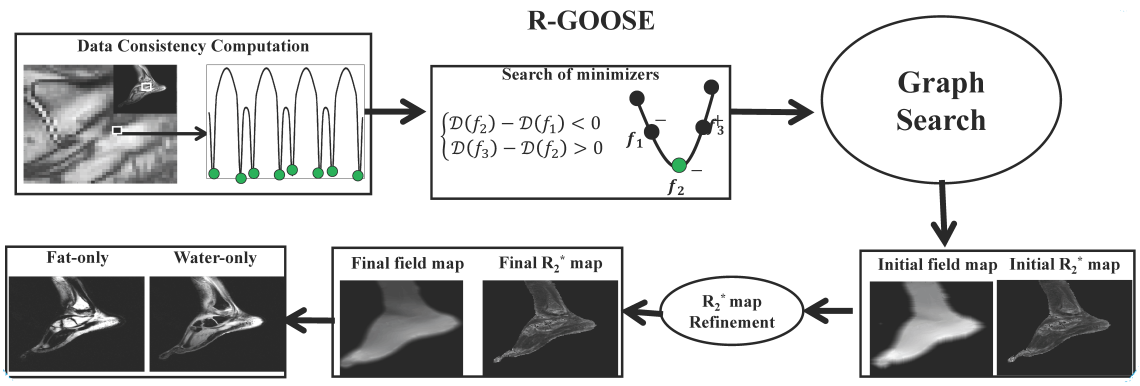

Figure 4.3: The information flow in the implementation of R-GOOSE. We discretize $\mathcal{D}(f(\mathbf{r}))$ in Eq.(5.2) on a uniform grid. Then we extract all minimizers (colorcoded in green) using finite difference method and import them to the graph model. The field map and the initial $R_2^* = 1/T_2^*$ map are obtained after the globally optimal surface estimation using the proposed smoothness penalized optimization formulation. The R_2^* are then updated in refinement using field map from graph search, which in conjunction with the field map is used for estimating fat water concentrations. The fat and water recovery can be achieved in steps after Graph Search.

up to 12 to ensure the coverage of the entire field inhomogeneity. 2) N_r, the number of discrete values of R_2^*. We use the search range of R_2^* as $0\,\mathrm{s}^{-1}$ to $500\,\mathrm{s}^{-1}$ with the number of discrete values $N_r = [2, 10, 20, 30, 40, 50, 60, 70, 80]$. 3) μ, the regularization parameter in Eq.(5.2). Similar to [41] and [59], the optimization is conducted in the range of $[0.01, 100]$.

Optimal parameters are determined by applying R-GOOSE with the above mentioned different values and benchmarking the quantitative scores with the reference in the first four uniformly sampled datasets. Note that the proposed framework can still be applied to non-uniformly sampled datasets such as dataset 3. Since the pattern of $\mathcal{D}(f(\mathbf{r}))$ for the non-uniformly sampled data is different from the uniformly sampled data, dataset 3 is not used to optimize N_f for the rest of uniformly sampled datasets in this experiment.

www.manaraa.com

4.5 Results

4.5.1 Parameter Optimization

The study of N_f with respect to the average score is shown in Fig.4.4(a). The average score starts to plateau around 9980 for R-GOOSE when $N_f = 8$. A better quantitative performance as N_f increases is because the field variation is not fully accounted for until $N_f = 8$. In Fig.4.4(b), the average score reaches the maximum around 9980 when N_r is larger than 30. Therefore, we chose $N_r = 30$ for the rest of the study. The average scores remain relatively unchanged between $\mu = 0.1$ and $\mu = 10$ in Fig.4.4(c). μ is set as 0.5 for the rest of experiments with the highest performance. The average run-time increases as the number of N_f goes bigger as in Fig.4.4.(d).

4.5.2 Comparison with GOOSE

In Fig.4.5, the liver dataset is challenging because the dome of the liver is surrounded by a signal void at the 2nd slice. This large low SNR region results in a swap in GOOSE and other state-of-the-art algorithms (See Chapter 3 Fig.3.7). In GOOSE, the difference between adjacent field map values is strictly set to be less than the hard constraint F in Eq.(4.1). However, the soft constraint as the smoothness penalty term in Eq.(5.2) in the proposed formulation permits a necessary 'jump' of field map from one node to its next. R-GOOSE successfully resolves the fat water swap as pointed by the arrow in the figure.

Table 4.1 shows quantitative scores and run-times from GOOSE (G) and R-

www.manaraa.com

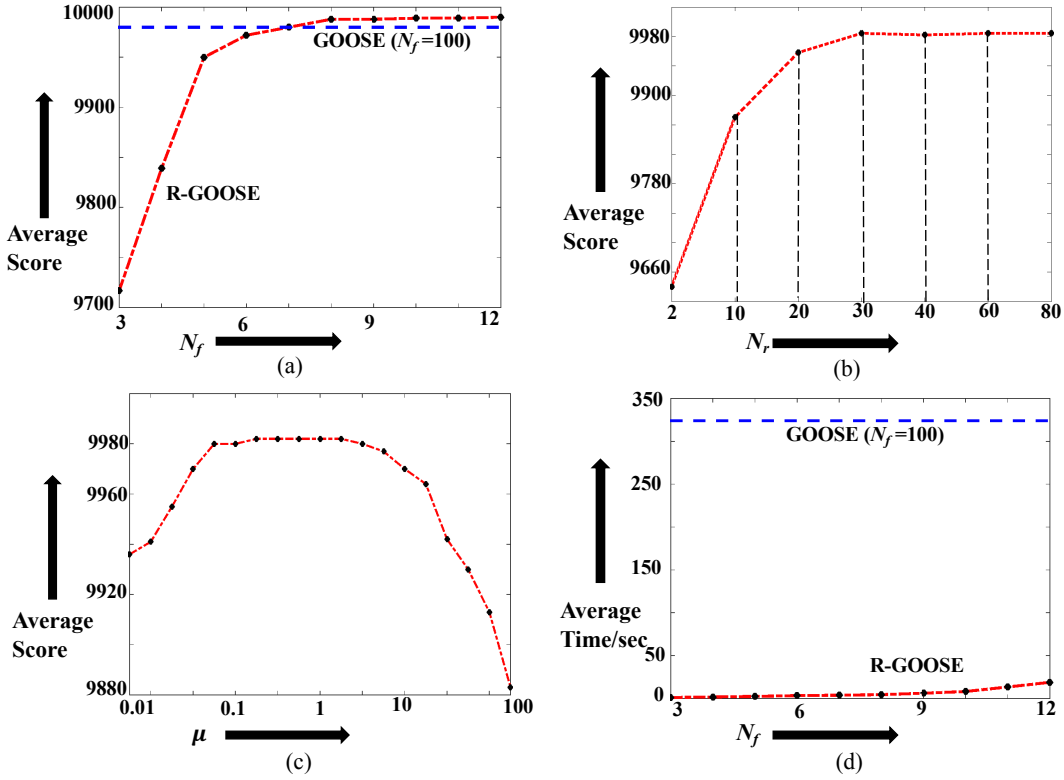

Figure 4.4: Dependence of the solution on the parameters. In (a), the change of the average score as a function of the number of layers (minimizers) N_f at 3 to 12 is plotted. The overall performance of R-GOOSE reaches the similar level as GOOSE (the dashed line) when $N_f = 9$. (b) is the plot for the averages score obtained from R-GOOSE as a function of the number of R_2^* points, N_r. Here, we use $N_f = 9$ and $\mu = 100$. We choose $N_r = 30$ for the rest of the experiments. N_r is observed to have little impact in computational time so the result of the time change with respect to N_r is not shown here. The score change with respect to the penalty parameter μ is shown in (c) for R-GOOSE. The scores are consistent across all N_f when μ is between [0.1, 2.0]. (d) is the plot for the relation between the average use of time and N_f. The average time of $N_f = 8$ is around 8 seconds and is reduced by an order of magnitude overall compared to GOOSE, the dotted line in the figure. Together with (a), we can see that R-GOOSE is able to achieve the same level of accuracy with at least 30 times of time saving in comparison with GOOSE.

GOOSE (RG) across the 17 datasets. As can be seen from the table, R-GOOSE obtain higher scores than GOOSE over the 17 datasets. The average run-time is 323 seconds for GOOSE while it is 8.1 for R-GOOSE. The new graph construction

www.manaraa.com

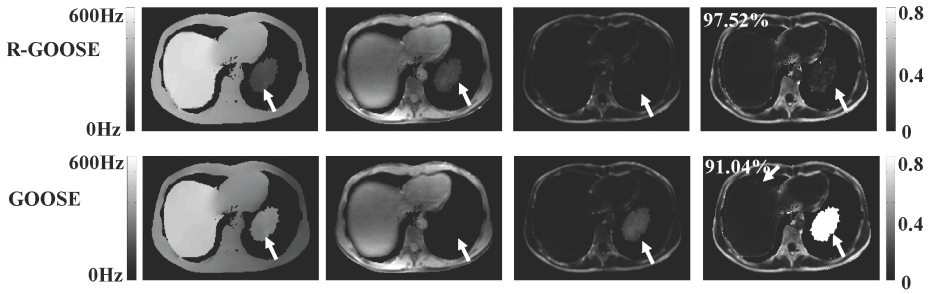

Figure 4.5: Qualitative comparisons between GOOSE and R-GOOSE on a liver dataset (2012 Challenge dataset 12). The fat fraction map shows that R-GOOSE resolves the swap while it remains in the the result from GOOSE. Overall, the proposed method outperforms GOOSE by more than 6% in quantitative scoring.

Method	Mean	1	2	3	4	5	6	7	8	9	10	11	12	13	14	15	16	17
Q(G)	99.27	99.84	99.81	96.50	99.87	99.94	99.88	99.90	99.94	99.97	99.72	99.75	95.58	99.91	99.87	99.15	99.13	98.80
Q(RG)	99.39	99.83	99.81	95.95	99.90	99.99	99.79	99.91	99.95	100.00	99.73	99.61	97.63	100.00	99.71	99.52	99.57	98.75
T(G)	323.9	220.7	183.5	269.2	319.1	318.8	160.8	314.4	700.9	829.3	224.9	536.7	522.4	192.4	422.7	76.7	154.8	59.4
T(RG)	8.1	9.1	8.3	9.1	10.5	14.5	10.9	10.6	9.4	7.1	8.9	4.2	10.2	2.3	9.5	7.4	2.7	3.5

Table 4.1: Quantitative and computational time comparisons of the proposed scheme against GOOSE. The first two rows are quantitative scores of GOOSE (Q(G)) and the proposed method (Q(RG)) for the 17 datasets. The last two rows are the computational time in seconds of graph search for GOOSE (T(G)) and the proposed method (T(RG)). Note that the scores of GOOSE are the summation of scores of multiple 2D single slices processed using GOOSE.

with the non-uniform spacing effectively mitigates this discretization error while also reducing the computational complexity in GOOSE.

4.6 Discussion

Similar to GOOSE, the proposed approach transforms the optimization problem to a surface estimation problem, but by only employing local minima in the graph construction. Each local minima is represented as a node in the graph and adjacent nodes in the graph are connected by edges with pre-defined weights. Specifically, our proposed approach has four distinct features:

www.manaraa.com

- The graph enables the existence of the non-uniform spacing between nodes, which reduces the number of layers in the graph by an order of magnitude (10-12 layers).

- Since the nodes (elements in the set of local minima) are non-uniformly spaced, a novel graph based surface estimation method [95] is introduced to solve the optimization problem. This new graph construction gives rise to significant reduction of edge connectivity in the graph.

- The employment of non-uniformly spaced nodes and the new graph construction result in fast computation and less memory demand in implementation.

- Furthermore, the proposed approach incorporates a smoothness term which penalizes the difference between two neighboring solutions using a quadratic penalty. Since we restrict the solutions to the local minima at each location, the algorithm is also robust to the selection of the smoothness regularization parameter.

In addition, similar to GOOSE, the proposed approach continues to obtain the global optimality of the final solution.

Meanwhile, the restriction of graph search to local minima also improves the accuracy of fat water recovery compared to GOOSE. In particular, R-GOOSE achieves full score in dataset 9 and 13. This is possible because the proposed method only chooses solutions from the exact minimizers, whereas GOOSE also considers possible field map values in the vicinity of the minimizers. In our experiment, the

www.manaraa.com

separation results are observed to be consistent and stable once the number of local minima N_f is larger than 8 at each location. With the high accuracy and reduced run-time, R-GOOSE can be potentially used in different applications such as Quantitative Susceptibility Mapping (QSM). R-GOOSE can be considered as an alternative to the current phase unwrapping procedure and the field inhomogeneity removal, through which a more accurate QSM can be obtained.

This smoothness-penalized optimization formulation in Eq.(5.2) is similar to [41], but the main difference here is the restriction of the feasible solutions at each pixel to the set LM($\mathbf{r}$). A similar strategy was used in [59], where the solutions are restricted to two local minima at each pixel. Since the quadratic pseudo boolean optimization (QPBO) algorithm in [59, 96] can only yield a partial solution, iterated conditional modes (ICM) [96] or multi-scale optimization was used [59] to ensure global convergence. However, we rely on a single-step algorithm (R-GOOSE) with guarantee of convergence to the global optimum of the cost function.

Though the proposed work has significantly reduced the memory demand for graph construction (100 layers to 9 layers per slice on average), one limitation of the proposed work is the memory requirement for hardware in solving large 3D cases. In order to perform a globally optimal search, the graph search method, by nature, is designed to include all entries of the set LM($\mathbf{r}$) at each pixel and the associated edge connectivity in the neighborhood of the pixel. With the edge connectivity among slices, the constructed 4D graph volume (3 spatial dimensions plus a 4th frequency dimension) will need larger memory storage than the summation of the 3D graph vol-

www.manaraa.com

umes at each slice. Therefore, a certain assessment for hardware capacity might be taken into account before the proposed method is applied on very large 3D datasets. One possible workaround is to reduce the size of LM($\mathbf{r}$) by only keeping entries with smallest data costs $\mathcal{D}(f(\mathbf{r}))$. This can be achieved by using techniques such as thresholding the data costs among all minimizers at each location.

4.7 Conclusion

In this chapter, a non-equidistant graph search model R-GOOSE is proposed in this work to improve the fully discretized model in our previous work GOOSE. With the new graph construction, the edge connectivity and number of nodes in the graph are reduced by an order of magnitude. In our experiments, R-GOOSE achieves slightly higher accuracy for fat water separation in ISMRM Challenge datasets, while the computation time is reduced by more than thirty times compared to GOOSE.

www.manaraa.com

CHAPTER 5
FAT WATER DECOMPOSITION USING MULTI-RESOLUTIONAL RAPID GLOBALLY SURFACE ESTIMATION (mR-GOOSE)

5.1 Introduction

From Chapter 3 to 4, we have introduced GOOSE, 3D-GOOSE and R-GOOSE three different graph search frameworks to solve for the MRI fat water separation problem. To the best of our knowledge, GOOSE is the first graph based algorithm that has achieved the global optimality of the pre-designed cost function without requiring an iterative approximating process like many previous methods. While still maintaining the global convergence of the smoothness regularized problem formulation, R-GOOSE utilizes a non-uniformly spaced graph model to avoid the connectivity contraint in the fully discretized graph model of GOOSE. The reduced graph size results in an order of magnitude improvement in computational efficiency, which is promising for possible clinical applications.

However, as we noted in Chapter 4 Discussion section, even though R-GOOSE is already among the fastest methods in field map estimation and fat-water separation, R-GOOSE may still face computational challenges both in terms of run-time and memory demand. The reasons are two-fold. First, as the technology advancement continues in MRI hardware, MRI datasets are growing towards 1) high resolution in spaital dimension, or an increase of size in $x-$ and $y-$ dimensions of the signal model, 2) high resolution in temporal dimension which can mean an increase of echo time, 3) full 3D scan of an anatomical region such as head or whole body, causing a

www.manaraa.com

larger number of slices, and 4) high field strength such as 7T, which transfers into an increase of size in the frequency dimension in the R-GOOSE graph model. It can also cause an increase of sheer value in cost function calculation which possibly requires a large data storage in computation. The other reason is, on the opposite, real clinical applications always appreciate a close-to-real-time fat water separation result while the scan is taking place.

Therefore, there is a strong motivation for further computation control. This chapter focuses on developing a new framework based on R-GOOSE that can further reduce the computational complexity, while still preserving the global convergence of the problem formulation. In this work, we continue to adopt the smoothness regularized formulation in R-GOOSE. However, we further exploit the field map smoothness in the vicinity of the local minima in spatial dimensions by creating a multi-resolutional pipeline in data flow. Optimal surface estimation is conducted twice, both at the original and a lower resolution of the voxel independent likelihood measurement. Both spatial and frequency dimensions are reduced in the steps of graph search, resulting in a further reduction of computational time.

Next, we first introduce the new information flow of the new framework from data input to the final outcome. Then we will explain the modifications of R-GOOSE formulation at the graph search steps of the multi-resolution framework. In the experiments, we will show the comparison between GOOSE, R-GOOSE and mR-GOOSE for both quantitative results and run-times. Finally, we conclude the chapter by discussing limitations of framework and possible improvements in future work.

www.manaraa.com

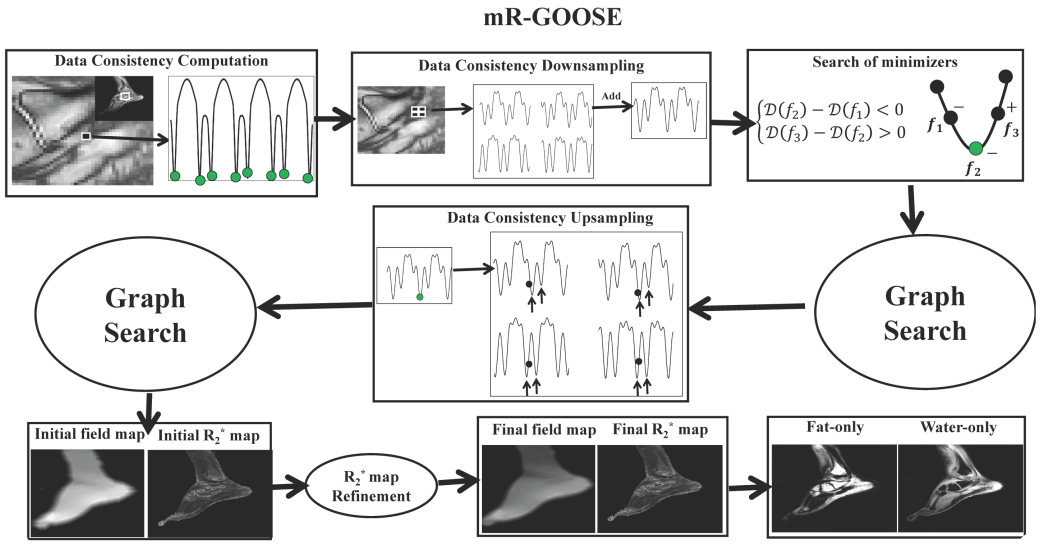

Figure 5.1: The information flow in the implementation of mR-GOOSE. In the multi-resolutional frame, the new downsampled $\mathcal{D}(f(\mathbf{r}))$ is computed as a summation of the local patch of the original data consistency. Once the initial field map is acquired from graph search, the set of minimizers is chosen to be the two candidates closest in frequency to the initial coarse estimate at each location. Then the final field map is refined by running the graph search for the second time. The fat and water recovery can be achieved in steps after Graph Search.

5.2 Multi-resolution Framework

Similar to Figure 4.2 in Chapter 4, Fig.5.1 illustrates the pipeline of data processing in the mR-GOOSE framework. As seen in the figure, there are two key differences in the mR-GOOSE framework compared to R-GOOSE: the Data Consistency Downsampling and Upsampling.

We now introduce these two steps respectively and draw connections to the data flow in R-GOOSE. First, we briefly review the steps in R-GOOSE. In R-GOOSE, we first determine $\mathrm{LM}(\mathbf{r})$, the set of local minima at the spatial location $\mathbf{r}$. By observing the change of sign for the finite differences of $\mathcal{D}\left(f(\mathbf{r})\right)$ in three consecutive field values in the frequency dimension, we decide whether the middle field value is a

www.manaraa.com

local minimum, shown as Search of Minimers in both Fig.4.2 in Chapter 4 and Figure 5.1. Once LM($\mathbf{r}$) is determined, we search for the optimal field map by solving the following smoothness penalized formulation:

$$\hat{f} = \arg\min_{f(\mathbf{r})} \sum_{\mathbf{r}} \left(\underbrace{\mathcal{D}(f(\mathbf{r}))}_{\text{data consistency}} + \mu \underbrace{\sum_{\mathbf{s}\in\mathcal{N}(\mathbf{r})} w_{\mathbf{rs}} |f(\mathbf{r}) - f(\mathbf{s})|^2}_{\text{smoothness regularization}} \right), \quad f(\mathbf{r}) \in \text{LM}(\mathbf{r}); \forall \mathbf{r} \quad (5.1)$$

$\mathcal{N}(\mathbf{r})$ in (5.1) denotes the local neighborhood of the voxel at location $\mathbf{r}$. $w_{\mathbf{rs}}$ are pre-defined weights that penalize the differences between field map values in the neighborhood $\mathcal{N}(\mathbf{r})$. μ is the regularization parameter that balances the data consistency term and smoonthness penalty term. The choices of $f(\mathbf{r})$ are limited to LM($\mathbf{r}$), the set of minimizers at location $\mathbf{r}$.

In mR-GOOSE, we first define a *downsampling window* as a non-overlapping square pixel neighborhood in the $x-$ and $y-$ spatial dimensions of the initial data consistency prior $\mathcal{D}(\mathbf{r})$. Then we subsample $\mathcal{D}(\mathbf{r})$ to obtain the new data consistency prior $\mathcal{E}(\mathbf{p})$ at a lower-resolution grid by summing up $\mathcal{D}(\mathbf{r})$ in the downsampling window:

$$\mathcal{E}(f(\mathbf{p})) = \sum_{\mathbf{s}\in\mathcal{M}(\mathbf{r})} \mathcal{D}(f(\mathbf{s})) \quad (5.2)$$

Here, $\mathcal{M}(\mathbf{r})$ is the downsampling window. Note that it is different from $\mathcal{N}(\mathbf{r})$. $\mathcal{N}(\mathbf{r})$ is the pre-defined voxel neighborhood where the smoonthness penalty is imposed between two connected nodes in the adjacent columns. The downsampling factor

www.manaraa.com

α(or the window size) is the length of a side of the downsampling window. An example of the downsampling process is shown in Fig.5.1, where the downsampled data consistency prior $\mathcal{E}(f(\mathbf{p}))$ is obtained from a 2 by 2 window in the original volume of $\mathcal{D}(\mathbf{r})$. Here, the downsampling factor is 2. After the local minima set $\mathrm{LM}(\mathbf{p})$ is identified by searching for the finite difference in the volume of $\mathcal{E}(f(\mathbf{p}))$, the graph search algorithm is performed by solving the modified smoothness regularized optimization problem:

$$\hat{f} = \arg\min_{f(\mathbf{p})} \sum_{\mathbf{p}} \left(\mathcal{E}(f(\mathbf{p})) + \mu \sum_{\mathbf{s}\in\mathcal{N}(\mathbf{p})} w_{\mathbf{rs}} |f(\mathbf{p}) - f(\mathbf{s})|^2 \right), \quad f(\mathbf{p}) \in \mathrm{LM}(\mathbf{p}); \forall \mathbf{p} \quad (5.3)$$

Note that the solution from graph search is not the final values for field map estimation. We assume the field map is smooth and therefore the graph search result from Eq.(5.1) can provide the vicinity of the final solution. In other words, the purpose of the Data Consistency Downsampling step is to obtain a coarse estimate of the final optimal field map values while the graph size is only $\frac{1}{\alpha^2}$ of the original setting as in R-GOOSE.

Next, we introduce the Data Consistency Upsampling step. After locating the vicinity of the final solution via the first graph search, we search for the *closest local minimizer* ($\mathrm{CLM}(\mathbf{r})$) neighbors of the field value in the corresponding low-resolution grid. Therefore, the optimization problem is modified to the following:

$$\hat{f} = \arg\min_{f(\mathbf{r})} \sum_{\mathbf{r}} \left(\mathcal{D}(f(\mathbf{r})) + \mu \sum_{\mathbf{s}\in\mathcal{N}(\mathbf{r})} w_{\mathbf{rs}} |f(\mathbf{r}) - f(\mathbf{s})|^2 \right), \quad f(\mathbf{r}) \in \mathrm{CLM}(\mathbf{r}); \forall \mathbf{r} \quad (5.4)$$

www.manaraa.com

Note that the number of entries N_{clm} in CLM($\mathbf{r}$) can vary depending on the specific data consistency prior $\mathcal{D}(\mathbf{r})$. It can also be affected by the accuracy of approximation from the low resolution graph search result, or in other words, the value of downsampling factor α. Once CLM($\mathbf{r}$) is determined, another graph search with only N_{clm} layers is conducted with a further reduction of computational time. The upsampling steps are also shown in Fig.5.1. With the final solution for field map after the second graph search, the following steps to optimize R_2^* and attain fat- and water-only maps are the same as in R-GOOSE.

5.3 Experiment Design

In order to maintain the consistency of signal model used in different frameworks, we continue to adopt the parameters of the reference signal model in the judging section of the 2012 ISMRM Challenge. Six fat spectral peaks model is used with the spectrum locations at δ_i = [-3.80, -3.40, -2.60, -1.94, -0.39, 0.60]ppm, with relative weights β_i = [0.0870, 0.6930, 0.1280, 0.0040, 0.0390, 0.0480]. Similarly, the single T_2^* constant is used at each voxel. The search of $1/T_2^* = R_2^*$ is separated as a preprocessing step before the first graph search, and is repeated with the obtained field map after the second graph search for optimization.

In this work, we compare the proposed mR-GOOSE framework with R-GOOSE and GOOSE by applying all three framworkds on the 17 datasets from 2012 ISMRM Challenge. The performance are judged based on both quantitative accuracy and computation time. The quantitative accuracy, or the score is determined by the

www.manaraa.com

percentage of pixels in the pre-defined mask in which the difference of fat fraction between the tested result and the reference is less than a threshold (0.1). All algorithms are computed on the Linux Workstation with 3.2 GHz Intel Xeon CPU and 23.6GB RAM to ensure the same computing capacity in hardware.

We also determined the validity of the proposed scheme and evaluate the computational savings compared to R-GOOSE on nine bilateral lower limb datasets with 0.7mm slices, acquired with a gradient-echo-based 3-point Dixon sequence. All nine datasets are of size $512 \times 240 \times 30$ in spatial dimensions and contain 3 echo time at [3.45, 4.60, 5.75]ms. mR-GOOSE is also tested on one quantitative susceptibility mapping (QSM) dataset. The dataset is collected on Siemans 3T scanner with 5.9ms echo time shift and size of $256 \times 256 \times 64$. More details can be found at [39]. Results from mR-GOOSE are compared with the orignal method in [39], where a region growing method is employed for field map estimation.

Two parameters need to be optimized in the proposed algorithm: 1) N_{clm}, the number of graph layers in the second search, or the number of entries in CLM . As we observed in R-GOOSE, the largest range of field inhomogeneity for all the 17 datasets is about $[0, 1020]$Hz in dataset 12 and contains up to 5 periods (about 12 minimizers). The maximum number of local minima in each period can be up to 4. Therefore, we test $N_f = 2$ up to 4 to ensure the coverage of all possible local minima in one period for the second graph search. 2) α, the downsampling factor. We test 4 values: $\alpha = 2, 4, 6, 8$ in this experiment. Since the graph search steps are identical to R-GOOSE, we adopt N_r, the number of discrete values of R_2^* from R-GOOSE.

www.manaraa.com

Similar to R-GOOSE, [41] and [59], μ is also independent from the datasets due to the smoothness regularized formulation. We again choose the optimal value obtained from R-GOOSE. Optimal parameters are also determined by applying mR-GOOSE with the above-mentioned different values and benchmarking the quantitative scores with the reference in the first four uniformly sampled datasets. Again, the proposed framework can still be applied to non-uniformly sampled dataset such as dataset 3. Since the pattern of $\mathcal{D}(f(\mathbf{r}))$ for the non-uniformly sampled data is different from the uniformly sampled data, dataset 3 is not used in optimization for the rest of uniformly sampled datasets in this experiment.

5.4 Results

5.4.1 Parameter Optimization

The study of α and N_{clm} with respect to the average scores and run times is shown in Table **??**. The average score starts to decrease when the downsampling factor reaches 6, even though the computation time is shortened to within 5 seconds. The number of the closest local minima N_{clm} seems to have little impact on the scores once α is chosen. However, the run time increases if N_{clm} goes higher. We choose $\alpha = 4$ and $N_{clm} = 2$ for the rest of the experiments since they provide the best performance on the first four uniformly sampled datasets.

5.4.2 Comparison with R-GOOSE and GOOSE

In Chapter 4, we showed the fat-water separation results for a live dataset from both GOOSE and R-GOOSE. This dataset presents a signal void at the dome of the

www.manaraa.com

α	N_{clm}	Score	Times
2	2	99.48	7.4
	3	99.47	8.2
	4	99.48	10.0
4	2	99.48	4.9
	3	99.46	5.5
	4	99.47	6.8
6	2	99.36	4.6
	3	99.33	4.9
	4	99.35	5.4
8	2	99.01	3.7
	3	99.12	4.2
	4	99.22	5.0

Table 5.1: Study of α and N_{clm} with respect to quantitative scores and running times.

object at the 2nd slice. This large low SNR region results in a swap in GOOSE and other state-of-the-art algorithms (See Chapter 3 Figure 3.7). In Fig. 5.2, we show the results from GOOSE, R-GOOSE and mR-GOOSE. Similar to R-GOOSE, the smoothness regularized formulation in Eq.(5.4) in the mR-GOOSE allows the sudden change of field map from one node to its next. mR-GOOSE also successfully resolves the fat water swap as pointed by the arrow in the figure. Table 5.2 shows quantitative scores and run times from GOOSE (G), R-GOOSE (RG) and mR-GOOSE (mRG) across the 17 datasets. mR-GOOSE obtain higher scores than both GOOSE and R-GOOSE over the 17 datasets. The average run time is 323 seconds for GOOSE, 8.1 for R-GOOSE and 4.5 for mR-GOOSE.

www.manaraa.com

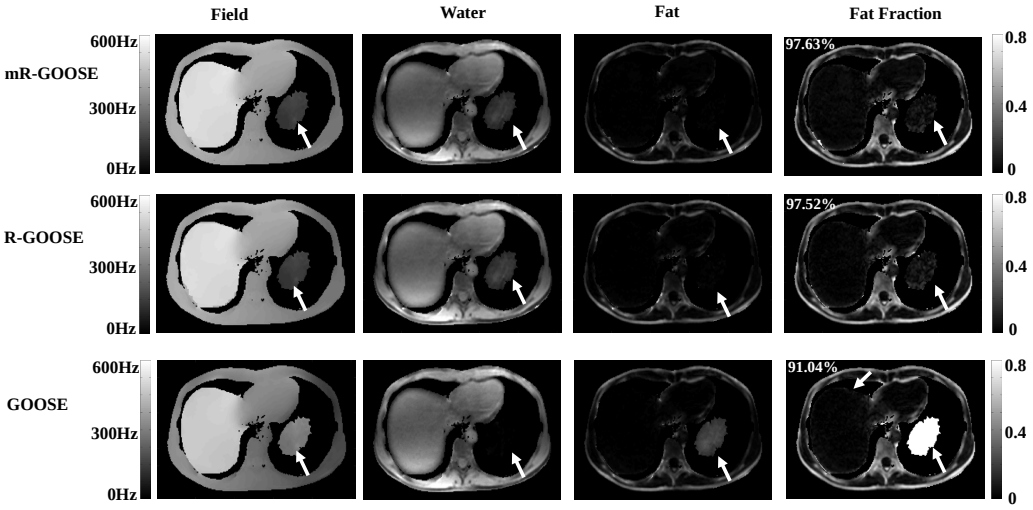

Figure 5.2: Qualitative comparisons between GOOSE, R-GOOSE, and mR-GOOSE on a liver dataset (2012 Challenge dataset 12). The fat fraction map shows that both R-GOOSE and mR-GOOSE resolve the swap while it remains in the the result from GOOSE. Overall, both mR-GOOSE and R-GOOSE outperform GOOSE by more than 6% in quantitative scoring.

Method	Mean	1	2	3	4	5	6	7	8	9	10	11	12	13	14	15	16	17
Q(G)	99.27	99.84	99.81	96.50	99.87	99.94	99.88	99.90	99.94	99.97	99.72	99.75	95.58	99.91	99.87	99.15	99.13	98.80
Q(RG)	99.39	99.83	99.81	95.95	99.90	99.99	99.79	99.91	99.95	100.00	99.73	99.61	97.63	100.00	99.71	99.52	99.57	98.75
Q(mRG)	99.46	99.84	99.83	96.12	99.89	100.00	99.87	99.91	100.00	100.00	99.88	99.79	97.75	100	99.72	99.69	99.67	98.93
T(G)	323.9	220.7	183.5	269.2	319.1	318.8	160.8	314.4	700.9	829.3	224.9	536.7	522.4	192.4	422.7	76.7	154.8	59.4
T(RG)	8.1	9.1	8.3	9.1	10.5	14.5	10.9	10.6	9.4	7.1	8.9	4.2	10.2	2.3	9.5	7.4	2.7	3.5
T(mRG)	4.5	4.2	4.8	3.6	5.1	5.5	5.0	5.8	3.6	4.6	4.7	5.6	4.9	2.7	5.0	4.8	3.3	3.2

Table 5.2: Quantitative and computational time comparisons of the proposed scheme against GOOSE. The first three rows are quantitative scores of GOOSE (Q(G)), R-GOOSE (Q(RG)) and mR-GOOSE (mRG) for the 17 datasets. The last three rows are the computational time in seconds of graph search for GOOSE (T(G)), R-GOOSE (T(RG)) and mR-GOOSE (T(mRG)). Note that the scores of GOOSE are the summation of scores of multiple 2D single slices processed using GOOSE.

Fig.5.4 shows results from the study on one of the bilateral lower limb datasets using mR-GOOSE and R-GOOSE. The purpose of this study is to evaluate fat fraction map as a biomarker for disease progression and treatment efficacy in degenerative muscle diseases such as myotonic dystrophy (DM1) and Charcot-Marie-Tooth disease (CMT), which are characterized by fatty infiltration as the muscle atrophies. The

www.manaraa.com

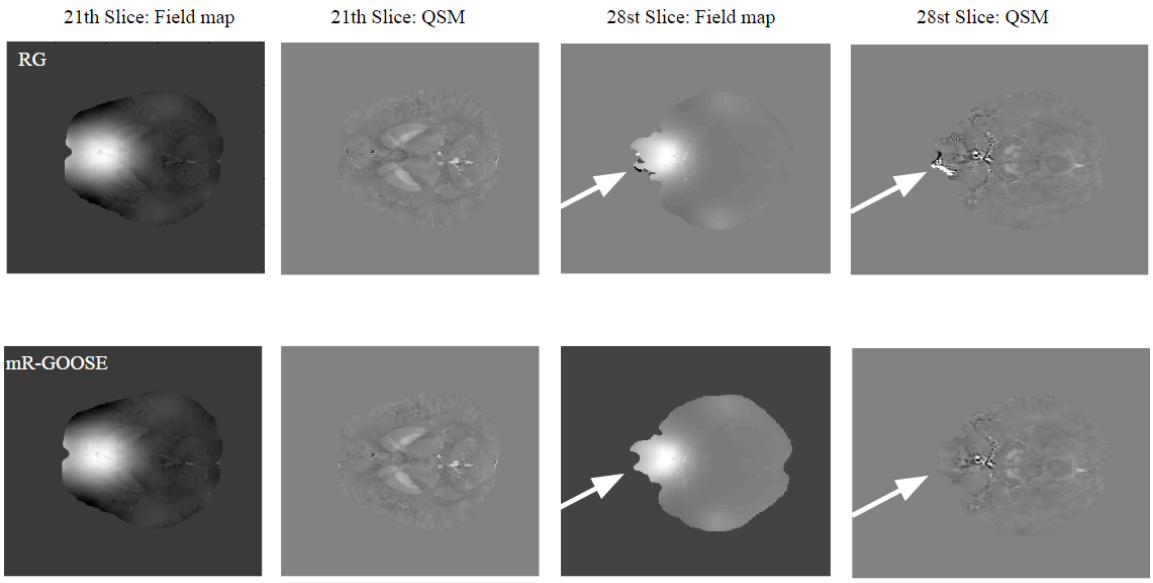

Figure 5.3: Comparison between mR-GOOSE and the region growing method on a QSM dataset using mR-GOOSE. The size of the data is 240*512*30. Fat, water and fat fraction maps of the 1st, 11th, 21st slices are shown. RG: region growing

running time is about 3 minutes for the dataset of size 512*240*30 without using the multi-resolution frame, while the processing time using mR-GOOSE is around 1 minute. Since the results from mR-GOOSE is almost identical to the one using R-GOOSE, we only show the ones from mR-GOOSE here.

Fig.5.3 shows results of field maps and QSM maps from both mR-GOOSE and the region growing method in [39]. Both mR-GOOSE and region growing provide correct results at the 21th slice. However, at the 28th slice, the region growing method generates a few artifacts (pointed by arrow) near the sinuous area while the field map obtained from mR-GOOSE are consistently smooth.

www.manaraa.com

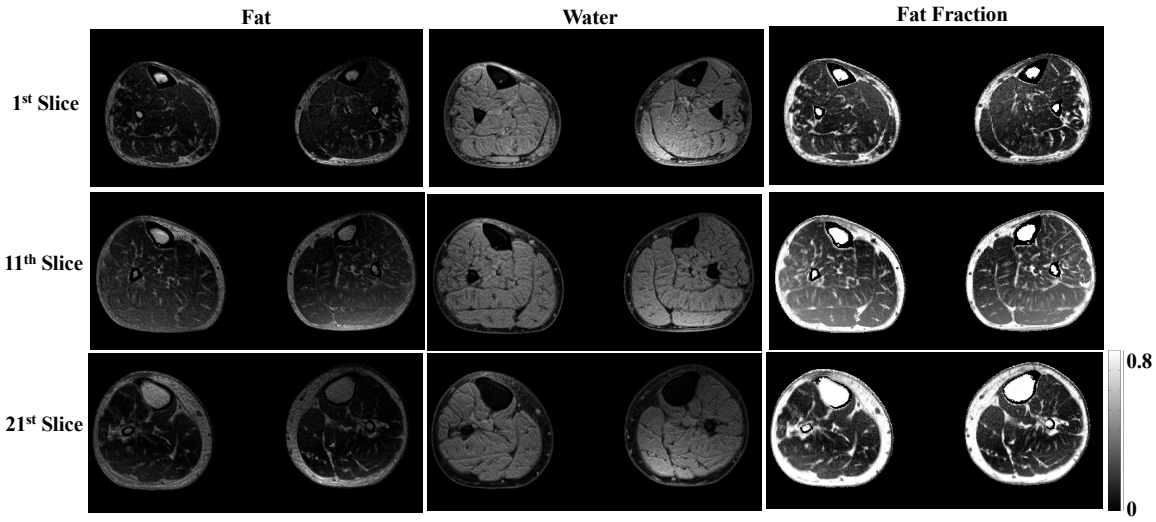

Figure 5.4: Results of a knee dataset using mR-GOOSE. The size of the data is 240*512*30. Fat, water and fat fraction maps of the 1st, 11th, 21st slices are shown.

5.5 Discussion

The proposed mR-GOOSE framework has two major advantages: 1) Through the multi-resolutional hierarchy, the complexity of the graph model is further lessened. Graph search is executed twice with a reduced size of graph each time resulting in another 50% computational savings compared to R-GOOSE. 2) The framework still maintains the global convergence of the optimization formulation. These two advantages guarantee a high level of accuracy and efficiency in fat water decomposition results.

The number of the closest local minima N_{clm} has little effect on the outcome of graph search. It is possibly because the coarse estimate from the first graph search is very close to the final solution. With the purpose of ensuring global optimality, one can also apply the thresholding technique to eliminate all local minima with relatively large data consistency prior. This will further constrain CLM to only contain the local

www.manaraa.com

minima with the highest likelihoood for global optimality.

The choice of downsampling factor α can be improved with more data validation. One concern for choosing a proper α is that the field smoothness assumption might not stand in certain cases. For example, in the live dataset (Fig.**??**), the signal void inside the object contains strong field variations particularly near the boundary of the void. Our experiment proves the results will contain artifacts or even fat water swaps if α is greater than 6. Therefore, a larger variety of datasets can be used to validate a more reliable choice of α.

As we note in Introduction, though GOOSE, R-GOOSE and mR-GOOSE benefit from the global optimality of cost functions to achieve high performance without an iterative process, the global convergence property alone will not guarantee the correct separation of water and fat, particularly in challenging datasets. Like all methods that rely on optimization, the cost function needs to be designed and optimized carefully to ensure that the global minimizers are free of fat-water swaps. The benefit of the proposed formulation is that the proposed scheme does not require additional steps to ensure global convergence and is not sensitive to initialization in many iterative methods. With the global convergence guarantee, the proposed algorithm is an excellent tool to improve the formulation of the energy function.

5.6 Conclusion

In this chapter, a new multi-resolutional framework mR-GOOSE is proposed to further improve the computational efficiency of fat water decomposition. Two

www.manaraa.com

steps of graph search at original and lower resolutions of the data consistency prior shorten the run time to half of R-GOOSE. The efficiency and global accuracy are demonstrated with both the 17 ISMRM Challenge datasets and 9 knee datasets with a much larger size.

www.manaraa.com

CHAPTER 6
CONCLUSIONS

6.1 Summary

The ability of MRI to simultaneously map multiple chemical species based on their different chemical shifts is of great clinical importance. Specifically, separating signals originating from water and fat has a number of important applications, both in cases where the goal is to remove the fat signal, as well as in cases where the fat signal itself is of diagnostic interest. However, fat water separation is difficult in the presence of large field inhomogeneities, convergence to local minima and high computational complexity. Additionally, quantitative fat water imaging requires careful design of the optimization formulation. This dissertation has studied the problem of fat water separation in MRI, including new formulation, optimization strategies and efficient implementation frameworks. The proposed methods have been characterized and proven theoretically, and validated using a variety of datasets.

In short, we have developed GlObally Optimal Surface Estimation (GOOSE), rapid GlObally Optimal Surface Estimation (R-GOOSE) and multi-resolutional R-GOOSE, three new approaches for addressing fat water separation problem in MRI. Specifically, we proposed that:

1. A new smoothness constrained formulation to implicitly incorporate the assumption of field map smoothness. A discretized field map volume was designed for the purpose of globally optimal surface estimation.

www.manaraa.com

2. A non-equidistant graph search model to replace the fully discretized volume in GOOSE. With the new graph construction, the edge connectivity and number of nodes in the graph are reduced by an order of magnitude.

3. A new multi-resolutional extension of graph search method to further improve the computational efficiency of fat water decomposition. Two steps of graph search at original and lower resolutions of the data consistency prior shorten the run time by half in R-GOOSE.

4. All developed methods tested on the 17 ISMRM Challenge datasets with high quantitative and qualitative accuracy. The computational efficiency is also well demonstrated through validation.

6.2 Future Work

The scope of work for this thesis mainly focuses on the fat water separation problem from the aspects of the signal modelling, optimization formulation design and algorithm implementation. However, the final outcome of fat- and water-only images is affected by many factors in the steps of data collection, image reconstruction as well as the post-processing fat-water separation methods. Therefore, possible directions of future work can be, but are not limited to the following:

1. A straightforward continuation of this thesis is a more rigorous validation of R-GOOSE and mR-GOOSE through a larger variety of experiments and datasets. So far we have majorly tested on the 17 ISMRM Challenge datasets and a few other datasets. It will take a much larger pool of datasets with different field

www.manaraa.com

strengths, anatomical regions, and possibly various pathological presentations on images for the further clinical impact.

2. Another direction of work can be the design of a new signal model and problem formulations (cost functions) to better account for the natural flaw in the Dixon model and the large field variations. In many different applications of quantification of fat signals, the different types of fat might require a more sophisticated model than the classic Dixon model. How to better account for T_2^* effect than a mere single T_2^* model at each pixel may also provide a better visualization of fat signals. Meanwhile, the global optimality provided by graph search methods have already proven to be a consistent and high performing characteristic for fat water separation. However, the global convergence alone does not gaurantee a correct separation result as discussed before. Possible new problem formulations with better accoutability for field inhomogeneity and ambiguity of the current model, in combination with the global optimality, will further improve the performance of fat and water separation methods.

3. Futhermore, current fat water separation methods are built on deterministic models such as least square fitting, energy minimization and regularization. It will have great research value to utilize other models such predictive ones in machine learning (deep learning) for the purpose of fat water separation.

4. Last but not least, besides the possible work in fat water separation methods, improvements in data acquisition and MRI image reconstruction can also

www.manaraa.com

improve the result of fat water separation. For example, different pulse sequences and k-space trajectories can have an important impact on the fat water separation method. It can be very insightful to conduct futher studies of the acquisition time and separation results by designing different pulse sequences as well as k-space trajectories.

www.manaraa.com

REFERENCES

[1] P. Rinck, "Magnetic resonance in medicine. the basic text-41. book of the european magnetic resonance forum," 2003.

[2] M. A. Bredella, P. F. Tirman, C. G. Peterfy, M. Zarlingo, J. F. Feller, F. W. Bost, J. P. Belzer, T. K. Wischer, and H. K. Genant, "Accuracy of T2-weighted fast spin-echo MR imaging with fat saturation in detecting cartilage defects in the knee: comparison with arthroscopy in 130 patients." *AJR Am J Roentgenol*, vol. 172, pp. 1073–1080, 1999.

[3] T. A. Bley, O. Wieben, C. J. François, J. H. Brittain, and S. B. Reeder, "Fat and water magnetic resonance imaging," *J Magn Reson*, vol. 31, pp. 4–18, 2010.

[4] H. H. Hu, H. Kim, K. S. Nayak, and M. I. Goran, "Comparison of Fat–Water MRI and Single-voxel MRS in the Assessment of Hepatic and Pancreatic Fat Fractions in Humans," *Obesity*, vol. 18, pp. 841–847, 2010.

[5] S. B. Reeder, P. M. Robson, H. Yu, A. Shimakawa, C. D. G. Hines, C. A. McKenzie, and J. H. Brittain, "Quantification of hepatic steatosis with MRI: the effects of accurate fat spectral modeling," *J Magn Reson*, vol. 29, pp. 1332–1339, 2009.

[6] S. B. Reeder, M. Markl, H. Yu, J. C. Hellinger, R. J. Herfkens, and N. J. Pelc, "Cardiac CINE imaging with IDEAL water-fat separation and steady-state free precession," *J Magn Reson*, vol. 22, pp. 44–52, 2005.

[7] S. B. Reeder, Z. Wen, H. Yu, A. R. Pineda, G. E. Gold, M. Markl, and N. J. Pelc, "Multicoil dixon chemical species separation with an iterative least-squares estimation method," *Magnetic Resonance in Medicine*, vol. 51, no. 1, pp. 35–45, 2004.

[8] B. A. Hargreaves, N. K. Bangerter, A. Shimakawa, S. S. Vasanawala, J. H. Brittain, and D. G. Nishimura, "Dual-acquisition phase-sensitive fat–water separation using balanced steady-state free precession," *Magnetic resonance imaging*, vol. 24, no. 2, pp. 113–122, 2006.

[9] J. P. Wansapura, "Abdominal fat–water separation with ssfp at 3 tesla," *Pediatric radiology*, vol. 37, no. 1, pp. 69–73, 2007.

www.manaraa.com

[10] C.-Y. Liu, C. A. McKenzie, H. Yu, J. H. Brittain, and S. B. Reeder, "Fat quantification with ideal gradient echo imaging: correction of bias from t1 and noise," *Magnetic resonance in medicine*, vol. 58, no. 2, pp. 354–364, 2007.

[11] J. Ma, "A single-point dixon technique for fat-suppressed fast 3d gradient-echo imaging with a flexible echo time," *Journal of Magnetic Resonance Imaging*, vol. 27, no. 4, pp. 881–890, 2008.

[12] M. Bydder, T. Yokoo, G. Hamilton, M. S. Middleton, A. D. Chavez, J. B. Schwimmer, J. E. Lavine, and C. B. Sirlin, "Relaxation effects in the quantification of fat using gradient echo imaging," *Magnetic resonance imaging*, vol. 26, no. 3, pp. 347–359, 2008.

[13] P. Kellman, D. Hernando, S. Shah, S. Zuehlsdorff, R. Jerecic, C. Mancini, Z.-P. Liang, and A. E. Arai, "Multiecho dixon fat and water separation method for detecting fibrofatty infiltration in the myocardium," *Magnetic resonance in medicine*, vol. 61, no. 1, pp. 215–221, 2009.

[14] S. B. Reeder, C. A. McKenzie, A. R. Pineda, H. Yu, A. Shimakawa, A. C. Brau, B. A. Hargreaves, G. E. Gold, and J. H. Brittain, "Water–fat separation with ideal gradient-echo imaging," *Journal of Magnetic Resonance Imaging*, vol. 25, no. 3, pp. 644–652, 2007.

[15] S. B. Reeder, A. R. Pineda, Z. Wen, A. Shimakawa, H. Yu, J. H. Brittain, G. E. Gold, C. H. Beaulieu, and N. J. Pelc, "Iterative decomposition of water and fat with echo asymmetry and least-squares estimation (ideal): application with fast spin-echo imaging," *Magnetic resonance in medicine*, vol. 54, no. 3, pp. 636–644, 2005.

[16] P. A. Hardy, R. S. Hinks, and J. A. Tkach, "Separation of fat and water in fast spin-echo mr imaging with the three-point dixon technique," *Journal of Magnetic Resonance Imaging*, vol. 5, no. 2, pp. 181–185, 1995.

[17] S. Fuller, S. Reeder, A. Shimakawa, H. Yu, J. Johnson, C. Beaulieu, and G. E. Gold, "Iterative decomposition of water and fat with echo asymmetry and least-squares estimation (ideal) fast spin-echo imaging of the ankle: initial clinical experience," *American Journal of Roentgenology*, vol. 187, no. 6, pp. 1442–1447, 2006.

[18] J. Ma, J. B. Son, Y. Zhou, H. Le-Petross, and H. Choi, "Fast spin-echo triple-echo dixon (fted) technique for efficient t2-weighted water and fat imaging," *Magnetic resonance in medicine*, vol. 58, no. 1, pp. 103–109, 2007.

www.manaraa.com

[19] J. Machann, C. Thamer, B. Schnoedt, M. Haap, H.-U. Haring, C. D. Claussen, M. Stumvoll, A. Fritsche, and F. Schick, "Standardized assessment of whole body adipose tissue topography by mri," *Journal of Magnetic Resonance Imaging*, vol. 21, no. 4, pp. 455–462, 2005.

[20] J. W. Goldfarb, "Fat-water separated delayed hyperenhanced myocardial infarct imaging," *Magnetic resonance in medicine*, vol. 60, no. 3, pp. 503–509, 2008.

[21] T. L. Krebs and B. J. Wagner, "Mr imaging of the adrenal gland: radiologic-pathologic correlation." *Radiographics*, vol. 18, no. 6, pp. 1425–1440, 1998.

[22] G. M. Israel, N. Hindman, E. Hecht, and G. Krinsky, "The use of opposed-phase chemical shift mri in the diagnosis of renal angiomyolipomas," *American Journal of Roentgenology*, vol. 184, no. 6, pp. 1868–1872, 2005.

[23] X. Li, J. F. Youngren, B. Hyun, G. K. Sakkas, K. Mulligan, S. Majumdar, U. B. Masharani, M. Schambelan, and I. D. Goldfine, "Technical evaluation of in vivo abdominal fat and imcl quantification using mri and mrsi at 3 t," *Magnetic resonance imaging*, vol. 26, no. 2, pp. 188–197, 2008.

[24] S. Schuchmann, C. Weigel, L. Albrecht, M. Kirsch, A. Lemke, G. Lorenz, R. Warzok, and N. Hosten, "Non-invasive quantification of hepatic fat fraction by fast 1.0, 1.5 and 3.0 t mr imaging," *European journal of radiology*, vol. 62, no. 3, pp. 416–422, 2007.

[25] P. Murphy, I. Rowland, L. Viviers, M. Brada, M. Leach, and A. Dzik-Jurasz, "Could assessment of glioma methylene lipid resonance by in vivo 1h-mrs be of clinical value?" *The British journal of radiology*, vol. 76, no. 907, pp. 459–463, 2003.

[26] N. Jagannathan, M. Singh, V. Govindaraju, P. Raghunathan, O. Coshic, P. Julka, and G. Rath, "Volume localized in vivo proton mr spectroscopy of breast carcinoma: variation of water–fat ratio in patients receiving chemotherapy," *NMR in biomedicine*, vol. 11, no. 8, pp. 414–422, 1998.

[27] R. Longo, P. Pollesello, C. Ricci, F. Masutti, B. J. Kvam, L. Bercich, L. S. Croce, P. Grigolato, S. Paoletti, B. De Bernard, *et al.*, "Proton mr spectroscopy in quantitative in vivo determination of fat content in human liver steatosis," *Journal of Magnetic Resonance Imaging*, vol. 5, no. 3, pp. 281–285, 1995.

[28] H. K. Hussain, T. L. Chenevert, F. J. Londy, V. Gulani, S. D. Swanson, B. J. McKenna, H. D. Appelman, S. Adusumilli, J. K. Greenson, and H. S. Conjeevaram, "Hepatic fat fraction: Mr imaging for quantitative measurement and displayearly experience," *Radiology*, vol. 237, no. 3, pp. 1048–1055, 2005.

www.manaraa.com

[29] N. Mennesson, J. Dumortier, V. Hervieu, L. Milot, O. Guillaud, J.-Y. Scoazec, and F. Pilleul, "Liver steatosis quantification using magnetic resonance imaging: a prospective comparative study with liver biopsy," *Journal of computer assisted tomography*, vol. 33, no. 5, pp. 672–677, 2009.

[30] T. Yokoo, M. Bydder, G. Hamilton, M. S. Middleton, A. C. Gamst, T. Wolfson, T. Hassanein, H. M. Patton, J. E. Lavine, J. B. Schwimmer, *et al.*, "Nonalcoholic fatty liver disease: diagnostic and fat-grading accuracy of low-flip-angle multi-echo gradient-recalled-echo mr imaging at 1.5 t," *Radiology*, vol. 251, no. 1, pp. 67–76, 2009.

[31] J. M. McGavock, I. Lingvay, I. Zib, T. Tillery, N. Salas, R. Unger, B. D. Levine, P. Raskin, R. G. Victor, and L. S. Szczepaniak, "Cardiac steatosis in diabetes mellitus," *Circulation*, vol. 116, no. 10, pp. 1170–1175, 2007.

[32] C.-Y. Liu, A. Redheuil, R. Ouwerkerk, J. Lima, and D. Bluemke, "Myocardial fat quantification using 2d dixon mri: feasibility study," *Journal of Cardiovascular Magnetic Resonance*, vol. 11, no. 1, p. P107, 2009.

[33] C.-Y. Liu, A. Redheuil, R. Ouwerkerk, J. A. Lima, and D. A. Bluemke, "Myocardial fat quantification in humans: evaluation by two-point water-fat imaging and localized proton spectroscopy," *Magnetic resonance in medicine*, vol. 63, no. 4, pp. 892–901, 2010.

[34] A. Haase, J. Frahm, W. Hanicke, and D. Matthaei, "1H NMR chemical shift selective (CHESS) imaging," *Physics in Medicine and Biology*, vol. 30, p. 341, 2000.

[35] C. H. Meyer, J. M. Pauly, A. Macovski, and D. G. Nishimura, "Simultaneous spatial and spectral selective excitation," *Magn Reson Med*, vol. 15, pp. 287–304, 2005.

[36] F. Schick, "Simultaneous highly selective MR water and fat imaging using a simple new type of spectral-spatial excitation," *Magn Reson Med*, vol. 40, pp. 194–202, 2005.

[37] G. M. Bydder, R. E. Steiner, L. H. Blumgart, S. Khenia, and I. R. Young, "MR imaging of the liver using short TI inversion recovery sequences." *J Computer Assisted Tomography*, vol. 9, p. 1084, 1985.

[38] W. T. Dixon, "Simple proton spectroscopic imaging." *Radiology*, vol. 153, pp. 189–194, 1984.

www.manaraa.com

[39] Y. Wang and T. Liu, "Quantitative susceptibility mapping (qsm): decoding mri data for a tissue magnetic biomarker," *Magnetic resonance in medicine*, vol. 73, no. 1, pp. 82–101, 2015.

[40] H. Yu, A. Shimakawa, C. A. McKenzie, E. Brodsky, J. H. Brittain, and S. B. Reeder, "Multiecho water-fat separation and simultaneous R2* estimation with multifrequency fat spectrum modeling," *Magn Reson Med*, vol. 60, no. 5, pp. 1122–1134, 2008.

[41] D. Hernando, P. Kellman, J. P. Haldar, and Z. P. Liang, "Robust water/fat separation in the presence of large field inhomogeneities using a graph cut algorithm," *Magn Reson Med*, vol. 63, pp. 79–90, 2010.

[42] G. H. Glover and E. Schneider, "Three-point Dixon technique for true water/fat decomposition with B0 inhomogeneity correction," *Magn Reson Med*, vol. 18, pp. 371–383, 2005.

[43] S. B. Reeder, A. R. Pineda, Z. Wen, A. Shimakawa, H. Yu, J. H. Brittain, G. E. Gold, C. H. Beaulieu, and N. J. Pelc, "Iterative decomposition of water and fat with echo asymmetry and least-squares estimation (IDEAL): Application with fast spin-echo imaging," *Magn Reson Med*, vol. 54, pp. 636–644, 2005.

[44] J. Berglund, L. Johansson, H. Ahlstrom, and J. Kullberg, "Three-point Dixon method enables whole-body water and fat imaging of obese subjects," *Magn Reson Med*, vol. 63, pp. 1659–1668, 2010.

[45] H. Yu, S. B. Reeder, A. Shimakawa, J. H. Brittain, and N. J. Pelc, "Field map estimation with a region growing scheme for iterative 3-point water-fat decomposition," *Magn Reson Med*, vol. 54, pp. 1032–1039, 2005.

[46] M. Jacob and B. P. Sutton, "Algebraic decomposition of fat and water in MRI," *IEEE Trans Med Imaging*, vol. 28, no. 2, pp. 173–184, 2009.

[47] A. S. Soliman, J. Yuan, K. K. Vigen, J. A. White, T. M. Peters, and C. A. McKenzie, "Max-ideal: A max-flow based approach for ideal water/fat separation," *Magnetic resonance in medicine*, vol. 72, no. 2, pp. 510–521, 2014.

[48] J. Liu and M. Drangova, "Method for b0 off-resonance mapping by non-iterative correction of phase-errors (b0-nice)," *Magnetic resonance in medicine*, vol. 74, no. 4, pp. 1177–1188, 2015.

[49] W. Lu and Y. Lu, "Jigsaw: Joint inhomogeneity estimation via global segment assembly for water–fat separation," *IEEE transactions on medical imaging*, vol. 30, no. 7, pp. 1417–1426, 2011.

www.manaraa.com

[50] W. Huh, J. Fessler, and A. Samsonov, "Water-fat decomposition with regularized field map," in *Proc. Intl. Soc. Mag. Reson. Med*, vol. 16, 2008, p. 1382.

[51] W. Lu and B. A. Hargreaves, "Multiresolution field map estimation using golden section search for water-fat separation," *Magn Reson Med*, vol. 60, pp. 236–244, 2008.

[52] J. Tsao and Y. Jiang, "Hierarchical IDEAL: Fast, robust, and multiresolution separation of multiple chemical species from multiple echo times," *Magn Reson Med*, vol. 70, pp. 155–159, 2012.

[53] B. D. Coombs, J. Szumowski, and W. Coshow, "Two-point dixon technique for water-fat signal decomposition with b0 inhomogeneity correction," *Magnetic resonance in medicine*, vol. 38, no. 6, pp. 884–889, 1997.

[54] T. E. Skinner and G. H. Glover, "An extended two-point dixon algorithm for calculating separate water, fat, and b0 images," *Magnetic resonance in medicine*, vol. 37, no. 4, pp. 628–630, 1997.

[55] D. C. Ghiglia and M. D. Pritt, *Two-dimensional phase unwrapping: theory, algorithms, and software*. Wiley New York, 1998, vol. 4.

[56] Q. Xiang and L. An, "Water-fat imaging with direct phase encoding," *J Magn Reson*, vol. 7, pp. 1002–1015, 2005.

[57] L. An and Q.-S. Xiang, "Chemical shift imaging with spectrum modeling," *Magnetic resonance in medicine*, vol. 46, no. 1, pp. 126–130, 2001.

[58] J. Tsao and Y. Jiang, "Hierarchical ideal: robust water–fat separation at high field by multiresolution field map estimation," in *Proceedings of the 16th Annual Meeting of ISMRM*, 2008, p. 653.

[59] J. Berglund and M. Skorpil, "Multi-scale graph-cut algorithm for efficient water-fat separation," *Magnetic Resonance in Medicine*, 2016.

[60] D. Hernando, J. P. Haldar, B. P. Sutton, J. Ma, P. Kellman, and Z. P. Liang, "Joint estimation of water/fat images and field inhomogeneity map," *Magn Reson Med*, vol. 59, pp. 571–580, 2008.

[61] K. Li, X. Wu, D. Chen, and M. Sonka, "Optimal surface segmentation in volumetric images-a graph-theoretic approach," *Pattern Analysis and Machine Intelligence, IEEE Transactions on*, vol. 28, no. 1, pp. 119–134, Jan 2006.

www.manaraa.com

[62] Y. Boykov and V. Kolmogorov, "An experimental comparison of min-cut/max-flow algorithms for energy minimization in vision," *Pattern Analysis and Machine Intelligence, IEEE Transactions on*, vol. 26, no. 9, pp. 1124–1137, 2004.

[63] Y. Boykov, O. Veksler, and R. Zabih, "Fast approximate energy minimization via graph cuts," *IEEE Trans Pattern Anal*, vol. 23, pp. 1222–1239, 2001.

[64] Y. Boykov and O. Veksler, "Graph cuts in vision and graphics: Theories and applications," *The Handbook of Mathematical Models in Computer Vision. Springer*, pp. 79–96, 2006.

[65] H. Ishikawa, "Exact optimization for markov random fields with convex priors," *IEEE Transactions on Pattern Analysis and Machine Intelligence*, vol. 25, pp. 1333–1336, 2003.

[66] M. P. Kumar, O. Veksler, and P. H. Torr, "Improved moves for truncated convex models," *J. Mach. Learn. Res.*, vol. 12, pp. 31–67, Feb. 2011.

[67] F. Malmberg, J. Lindblad, N. Sladoje, and I. Nyström, "A graph-based framework for sub-pixel image segmentation," *Theoretical Computer Science*, vol. 412, no. 15, pp. 1338–1349, 2011.

[68] X. Wu and D. Z. Chen, "Optimal net surface problems with applications," in *Automata, Languages and Programming*. Springer, 2002, pp. 1029–1042.

[69] K. Lee, M. Niemeijer, M. K. Garvin, Y. H. Kwon, M. Sonka, and M. D. Abramoff, "Segmentation of the optic disc in 3-d oct scans of the optic nerve head," *Medical Imaging, IEEE Transactions on*, vol. 29, no. 1, pp. 159–168, 2010.

[70] Q. Song, Y. Liu, Y. Liu, P. K. Saha, M. Sonka, and X. Wu, "Graph search with appearance and shape information for 3-d prostate and bladder segmentation," in *Medical Image Computing and Computer-Assisted Intervention–MICCAI 2010*. Springer, 2010, pp. 172–180.

[71] S. Sun, M. Sonka, and R. R. Beichel, "Lung segmentation refinement based on optimal surface finding utilizing a hybrid desktop/virtual reality user interface," *Computerized Medical Imaging and Graphics*, vol. 37, no. 1, pp. 15–27, 2013.

[72] H. Zhang, A. K. Abiose, D. Gupta, D. N. Campbell, J. B. Martins, M. Sonka, and A. Wahle, "Novel indices for left-ventricular dyssynchrony characterization based on highly automated segmentation from real-time 3-d echocardiography," *Ultrasound in medicine & biology*, vol. 39, no. 1, pp. 72–88, 2013.

www.manaraa.com

[73] C. Bauer, M. A. Krueger, W. J. Lamm, B. J. Smith, R. W. Glenny, and R. R. Beichel, "Airway tree segmentation in serial block-face cryomicrotome images of rat lungs," *Biomedical Engineering, IEEE Transactions on*, vol. 61, no. 1, pp. 119–130, 2014.

[74] M. K. Garvin, M. D. Abràmoff, X. Wu, S. R. Russell, T. L. Burns, and M. Sonka, "Automated 3-d intraretinal layer segmentation of macular spectral-domain optical coherence tomography images," *Medical Imaging, IEEE Transactions on*, vol. 28, no. 9, pp. 1436–1447, 2009.

[75] M. D. Abràmoff, M. K. Garvin, and M. Sonka, "Retinal imaging and image analysis," *Biomedical Engineering, IEEE Reviews in*, vol. 3, pp. 169–208, 2010.

[76] S. Kashyap, Y. Yin, and M. Sonka, "Automated analysis of cartilage morphology," in *Biomedical Imaging (ISBI), 2013 IEEE 10th International Symposium on*. IEEE, 2013, pp. 1300–1303.

[77] Q. Song, X. Wu, Y. Liu, M. Smith, J. Buatti, and M. Sonka, "Optimal graph search segmentation using arc-weighted graph for simultaneous surface detection of bladder and prostate," *Medical Image Computing and Computer-Assisted Intervention–MICCAI 2009*, pp. 827–835, 2009.

[78] P. Hua, Q. Song, M. Sonka, E. A. Hoffman, and J. M. Reinhardt, "Segmentation of pathological and diseased lung tissue in ct images using a graph-search algorithm," in *Biomedical Imaging: From Nano to Macro, 2011 IEEE International Symposium on*. IEEE, 2011, pp. 2072–2075.

[79] D. Han, J. Bayouth, Q. Song, A. Taurani, M. Sonka, J. Buatti, and X. Wu, "Globally optimal tumor segmentation in pet-ct images: a graph-based cosegmentation method," in *Information Processing in Medical Imaging*. Springer, 2011, pp. 245–256.

[80] A. Shah, J. Bai, Z. Hu, S. Sadda, and X. Wu, "Multiple surface segmentation using truncated convex priors," in *International Conference on Medical Image Computing and Computer-Assisted Intervention*. Springer, 2015, pp. 97–104.

[81] M. Chen, J. Bai, Y. Zheng, and R. Siochi, "3d lung tumor motion model extraction from 2d projection images of mega-voltage cone beam ct via optimal graph search," *Medical Image Computing and Computer-Assisted Intervention–MICCAI 2012*, pp. 239–246, 2012.

www.manaraa.com

[82] Y. Yin, X. Zhang, R. Williams, X. Wu, D. D. Anderson, and M. Sonka, "Logismoslayered optimal graph image segmentation of multiple objects and surfaces: cartilage segmentation in the knee joint," *Medical Imaging, IEEE Transactions on*, vol. 29, no. 12, pp. 2023–2037, 2010.

[83] Q. Song, J. Bai, M. K. Garvin, M. Sonka, J. M. Buatti, and X. Wu, "Optimal multiple surface segmentation with shape and context priors," *Medical Imaging, IEEE Transactions on*, vol. 32, no. 2, pp. 376–386, 2013.

[84] Q. Song, J. Bai, M. K. Garvin, M. Sonka, J. M. Buatti, and X. Wu, "Optimal multiple surface segmentation with shape and context priors," *IEEE transactions on medical imaging*, vol. 32, no. 2, pp. 376–386, 2013.

[85] T. H. Cormen, C. E. Leiserson, R. L. Rivest, and C. Stein, *Introduction to algorithms*. MIT press, 2001.

[86] H. Ishikawa, "Exact optimization for Markov random fields with convex priors," *IEEE Trans Pattern Anal*, vol. 25, pp. 1333–1336, 2003.

[87] V. Kolmogorov and R. Zabin, "What energy functions can be minimized via graph cuts?" *IEEE Trans Pattern Anal*, vol. 26, pp. 147–159, 2004.

[88] K. Li, X. Wu, D. Z. Chen, and M. Sonka, "Optimal surface segmentation in volumetric images-a graph-theoretic approach," *IEEE Trans Pattern Anal*, vol. 28, pp. 119–134, 2006.

[89] X. Wu and D. Chen, "Optimal net surface problems with applications," *Automata, Languages and Programming*, vol. 2380, pp. 1029–1042, 2002.

[90] D. S. Hochbaum, "A new—old algorithm for minimum-cut and maximum-flow in closure graphs," *Networks*, vol. 37, pp. 171–193, 2001.

[91] J. C. Picard, "Maximal closure of a graph and applications to combinatorial problems," *Management Science*, vol. 22, pp. 1268–1272, 1976.

[92] M. Jacob, T. Blu, and M. Unser, "Efficient energies and algorithms for parametric snakes," *IEEE Trans Image Proc*, vol. 13, pp. 1231–1244, 2004.

[93] S. S. David, B. Johan, K. Joel, A. Hakan, J. A. Malcolm, and W. Brian, "Optimization of Fat-Water Separation Algorithm Selection and Options Using Image-based Metrics with Validation by ISMRM Fat-Water Challenge Datasets," in *Proceedings of the 21st Annual Meeting of ISMRM, Salt Lake City, UT*, 2013.

www.manaraa.com

[94] C. Cui, X. Wu, J. D. Newell, and M. Jacob, "Fat water decomposition using globally optimal surface estimation (goose) algorithm," *Magn Reson Med*, vol. 73, no. 3, pp. 1289–1299, 2015.

[95] A. Shah, J. Bai, M. D. Abramoff, and X. Wu, "Optimal multiple surface segmentation with convex priors in irregularly sampled space," *arXiv preprint arXiv:1611.03059*, 2016.

[96] J. Berglund and J. Kullberg, "Three-dimensional water/fat separation and t2* estimation based on whole-image optimizationapplication in breathhold liver imaging at 1.5 t," *Magnetic Resonance in Medicine*, vol. 67, no. 6, pp. 1684–1693, 2012. [Online]. Available: http://dx.doi.org/10.1002/mrm.23185

www.manaraa.com